Bohr, 1913-2013, Séminaire Poincaré XVII (2013) 59 – 97

Séminaire Poincaré

Bohr's Legacy in Cavity QED

Serge Haroche, Jean-Michel Raimond
LKB, ENS, 24 rue Lhomond, 75005, Paris, France
Collège de France, 11 Place Marcellin Berthelot, 75005, Paris, France

Abstract. Bohr played a central role in the interpretation of quantum mechanics. He based many discussions of its strange consequences on thought experiments. He imagined moving slit interferometers, able to record which path information, he played with photon boxes, storing photons for such long times that they could be weighed. The technological progress provided by quantum physics itself now make it possible to realize some of these thought experiments. We describe in this paper a few experiments based on microwave Cavity Quantum Electrodynamics (CQED) techniques. We trap photons in boxes and weigh them with scales at the atomic level. We are able to count the number of photons in the box without absorbing them in an ideal Quantum Non Demolition measurement of the field intensity. We can record which-path information in an atomic interferometer and directly illustrate complementarity. We can also prepare mesoscopic quantum superpositions reminiscent of the famous Schrödinger cat. We can get insight into the decoherence of these states and into ways to protect them, for instance by quantum feedback strategies.

1 Introduction

This Poincaré seminar celebrates the hundredth anniversary of Bohr's model. Introducing Planck's discontinuity hypothesis in a planetary atomic model, Bohr has been able to predict for the first time the atomic line frequencies, that eluded any classical interpretation so far. The Bohr's atom could emit or absorb radiation during a rather mysterious "quantum jump" between its quantized levels, leading to the emission or absorption of a photon with the energy of the atomic transition.

The Bohr model did not led to a full-fledged atomic level theory, in spite of the heroic efforts of Bohr, Sommerfeld and others. The final solution to the atomic spectra clue was provided by the birth of modern quantum theory, a few years later. John Heilbron's contribution to this Volume will certainly cover this rich and complex history. Even if the name of Bohr is not associated to one of the main laws of quantum physics, as those of Heisenberg, Schrödinger, Dirac or Born, his role in the development of the theory and of its interpretation has been considerable.

The founding fathers lifted the veil over a rather counter-intuitive quantum world. The basic quantum phenomena, like state superposition, indeed escape any simple interpretation in terms of our macroscopic world common experience. There are, as Schrödinger once stated, many 'ridiculous' consequences of the quantum theory. Perhaps for the first time in the history of physics, the theory required an interpretation layer to link the mathematical objects of the formalism to the experimental observations.

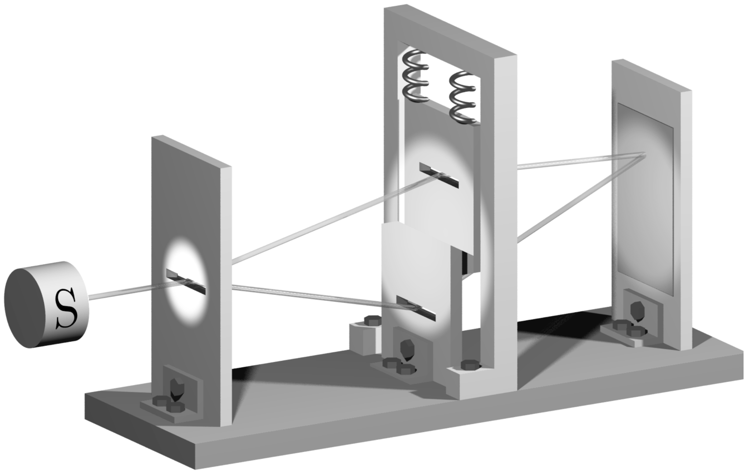

Figure 1: Boh's moving slit interferometer.

The standard 'Copenhagen' interpretation was mainly established under the impetus and supervision of Bohr [1]. His (sometimes heated) discussions with colleagues (like Einstein) led to an increasingly clear and sound formulation of the quantum theory. These discussions often relied on the discussion of thought experiments. They enhanced the quantum phenomena up to a point where they could be grasped more intuitively.

The Heisenberg microscope proposed to locate a single electron with light, for a discussion of the unavoidable momentum perturbation due to a position measurement. Bohr proposed the moving slit interferometer (Fig. 1) to illustrate the rather complex concept of complementarity [2]. In this simple case, the moving slit recoils when diffracting the interfering particle. It thus records a 'which path' information. The final motional state of the slit ideally unambiguously indicates the path followed by the particle in the interferometer. By a careful examination of Heisenberg uncertainty relations, Bohr concluded that the interference fringes then disappear. The particle (localized path) and wave (interference) characters of the quantum object cannot be observed simultaneously.

Another striking example of thought experiment is the 'photon box' (Fig. 2) imagined by Einstein and Bohr [3], once again in a heated debate on the Heisenberg uncertainty relations. They envisioned a box, covered with perfect mirrors, that could hold a photon for an arbitrary lapse of time. Weighing the box allows one to monitor the presence of the photon and to precisely determine its energy. The clockwork mechanism was supposed to leave the photon escape at a precisely defined time. About ten years later, Einstein and Bohr again debated the Einstein-Podoldsky-Rosen situation [4, 5] illustrating in a vivid way the mind-bogging non-local character of quantum physics.

Under the guidance of Bohr, quantum theory got a firm standing and a clear, if counter-intuitive, interpretation. It led very rapidly to considerable developments. In less than 20 years, its founding fathers got an almost complete understanding of the bases of atomic, molecular and solid state physics. Immediately after World War II, the renormalization procedures allowed one to treat consistently quantum electrodynamics, providing us with one of the most predictive and precise physical

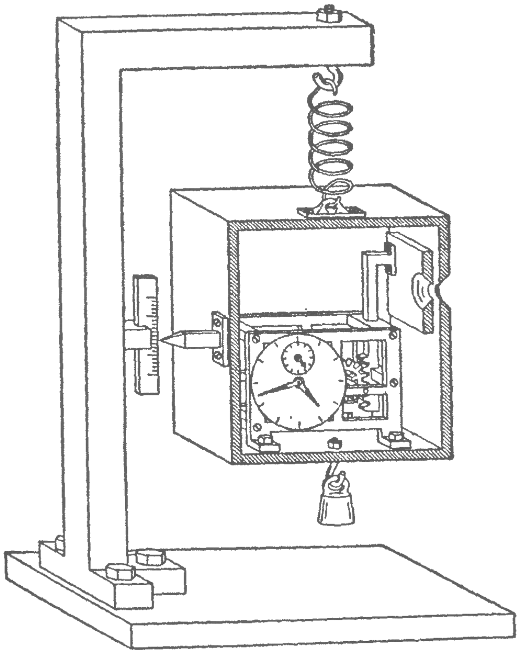

Figure 2: The photon box.

theories so far.

The rise of the quantum also led to an impressive number of practical applications, with considerable societal and economical impact. The quantum understanding of solid-state conduction led eventually to the transistors, to the integrated circuits and finally to the modern computers and information processing devices. The quantum atom-field interaction led to the development of lasers, and hence of the fast communication technology. Atomic laser cooling and the Ramsey interferometric method [6], led to atomic clocks with such a precision that they would drift only by a few seconds over the full age of the universe [7]. Medical diagnostic also benefited considerably from the quantum with the MRI imaging [8], which relies on the quantum dance of nuclear spins in the magnetic field provided by a superconducting magnet, yet another quantum technology. A large fraction of our societies GDP, a large fraction of our own life expectancy, thus rely on technologies deriving directly from the quantum.

Of course, these developments had also a major impact on experimental physics. With lasers, computers and superconducting devices, we achieve an unprecedented level of control on the experiments. It is now possible to manipulate directly individual quantum systems, carefully screened from the parasitic influence of their environment. In other words, we are now able to realize some of the thought experiments proposed by Bohr and the founding fathers. We can operate single particle interferometers, we can store photons in boxes and weigh them, we can study non-local quantum states. These fascinating possibilities led to a considerable surge of interest for fundamental quantum physics, in a wide range of domains, from atomic physics and quantum optics to condensed matter physics.

Why should we devote efforts to these 'thought experiments made real', nearly a century after they were proposed? First because they put our understanding of the quantum in direct scrutiny. Realizing these experiments and finding that they indeed provide the expected 'ridiculous consequences' is the most stringent test quantum physics could pass. We can also use these situations to explore the limits of the quantum world. One of the main open questions is why the weird quantum features never emerge at our scale. There are no conspicuous non-local effects, even no state superpositions at our scale. This problem was vividly illustrated by Schrödinger in yet another famous thought experiment [9], in which an unfortunate cat was cast in a superposition of her dead and alive states. We can experiment with mesoscopic quantum systems and prepare them in state superpositions reminiscent of this cat's fate. We can directly study the decoherence mechanism transforming very rapidly these state superpositions into mere statistical mixtures.

Beyond such fundamental questions, these experiments also open the way to new applications of the quantum. Quantum-enabled metrology is promising for more precise clocks or sensors. Quantum information transmission and processing achieve feats beyond the reach of standard binary machines. In particular, quantum simulation opens fascinating routes for a better understanding of complex quantum systems.

Experiments on basic quantum physics is thus a thriving field worldwide. Cavity Quantum Electrodynamics (CQED) [10] belongs to this trend. It focuses on the matter-field coupling in the most extreme situation, where all matter has been removed but the last atom. The field is reduced to a single mode, stored in a high quality cavity, a modern equivalent of the Einstein-Bohr photon box. This mode contains only a few photons, one photon or even no photon at all. This situation implements thus one of the simplest non-trivial quantum systems, a spin-1/2 (the two-level atom) coupled to a one-dimensional harmonic oscillator (the mode). The experimental observations can thus be interpreted directly in terms of the most basic quantum postulates and can illustrate the most fundamental quantum behaviours.

Cavity QED has already a long history, starting from a seminal remark by Purcell [11] about the possibility to alter the spontaneous emission rate by imposing limiting conditions to the electromagnetic continuum. It now focuses on the 'strong coupling' regime, where the coherent atom-field coupling overwhelms the dissipative processes (atomic spontaneous emission or cavity losses). Cavity QED now comes in a variety of flavours [12]. Optical cavity QED studies atomic optical transitions coupled to cavities, for instance open Fabry Perot. It has important possible applications as a light-matter interface for quantum information transmission [13]. Solid state cavity QED couples artificial atoms, quantum dots for instance, to integrated cavities, with a considerable potential for applications [14]. The recent flavour of circuit-QED uses artificial atoms made up of superconducting circuits coupled to superconducting stripline resonators or closed cavity modes [15].

This Chapter will be devoted to the microwave Cavity QED flavour. It uses circular Rydberg atoms coupled to extremely high-Q superconducting cavities. The damping rate of both the atomic and field systems are extremely low, making it possible to achieve interesting quantum situations and to illustrate some of the original Bohr's proposals.

We will start, in Section 2 by rapidly reviewing the main tools of microwave CQED. We will in particular focus on the circular Rydberg atoms, which are the atomic levels closest to the Bohr's model. We will see that, according to Bohr's correspondence principle, nearly all of their properties can be computed classically.

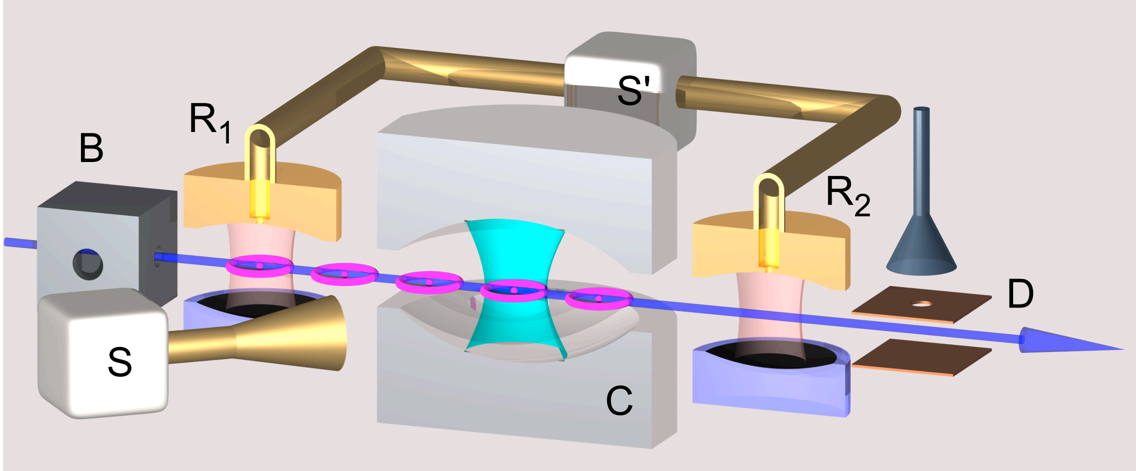

Figure 3: Scheme of the microwave CQED experiments.

They are nevertheless ideal tools to unveil the quantum. We will also describe in this Section the Jaynes and Cummings model [16] describing the coherent atom-field coupling and we will give the master equation used to treat field relaxation.

The next Section (3) will be devoted to a very direct illustration of the original concept of quantum jumps. We will show that atoms, crossing one by one the cavity mode, can provide Quantum Non Demolition information about the photon number [17, 18]. We can use their detection at the exit of a Ramsey atomic interferometer to count the number of photons in the cavity without destroying them. This ideal photo-detection process obeys all postulates for a quantum measurement. It allows us to follow in real time the number of photons and to evidence the quantum jumps of light when photons escape, due to the unavoidable residual cavity losses. The statistical study of these jumps [19] provides an extremely stringent test of quantum relaxation models. We will also show that, using a quantum feedback scheme, we can counteract the effect of these jumps and maintain a constant photon number in the mode in spite of cavity losses [20, 21].

The last Section (4) deals with Bohr's complementarity, in a situation strongly reminiscent of the moving-slit interferometer (Fig. 1). We use a mesoscopic coherent field in the cavity as a path-recording device in the atomic Ramsey interferometer and show that interference and which-path information are incompatible [22]. We will show that the final field state in this experiment is a mesoscopic quantum superposition quite reminiscent of the famous Schrödinger cat. Monitoring the evolution of the cavity state by a variant of the QND procedure [23], we will be able to observe directly the decoherence process transforming rapidly this superposition into a mere statistical mixture. Section 5 will conclude this paper and present some perspectives for microwave cavity QED.

2 The tools of microwave CQED

The general scheme of our microwave cavity QED experiments is presented in Fig. 3. The circular Rydberg atoms are prepared by laser and radio-frequency excitation of a velocity-selected thermal rubidium beam in the box B (atomic velocity

$v = 250$ m/s). The atoms interact with the field stored in the open Fabry-Perot superconducting cavity C. A coherent field can be injected in the cavity by the source S, coupled to the cavity mode by diffraction on the mirrors edges. The atoms are finally detected by efficient state-selective field ionization in D. Classical resonant microwave pulses applied by the source S' in the two low-Q cavities R_1 and R_2 can be used to manipulate the atomic state before or after the interaction with C. With $\pi/2$ pulses in R_1 and R_2, we realize a Ramsey atomic interferometer. We will now briefly review the main components of this set-up, starting with the circular Rydberg atoms.

2.1 Circular Rydberg atoms: the Bohr model revived

A circular Rydberg state [24, 25] is a very high-lying alkali atom level, in which the single valence electron has been excited close to the ionization limit, in a state with a large principal quantum number n and a maximum value $\ell = |m| = n - 1$ for the orbital, ℓ, and magnetic, m, quantum numbers (ℓ and m are defined with respect to the quantization axis Oz). This state will be denoted $|nC\rangle$. Typically, in our experiments we use two adjacent circular levels with principal quantum numbers 51 and 50, that we will also denote $|e\rangle = |51C\rangle$ and $|g\rangle = |50C\rangle$.

The electron orbits at distances much larger than the size of the singly charged ionic core of the alkali atom, which has a diameter of the order of a_0 and the electronic structure of a noble gas (krypton for rubidium). To an excellent approximation, this core behaves as a point charge, creating a nearly perfect $1/r$ potential for the valence electron. The energy of the circular states is thus given by the hydrogenic expression:

$$E_n = -\frac{R}{n^2} \ , \tag{1}$$

where R is the Rydberg constant (we neglect for this simple discussion the contribution of the finite core mass).

The spherical harmonic of maximum ℓ and m values take a simple form, leading to the circular state wave function in spherical coordinates:

$$\Psi(r,\theta,\phi) = \frac{1}{(\pi a_0^3)^{1/2}}\frac{1}{n^n n!}\left(-\frac{r}{a_0}\sin\theta e^{i\phi}\right)^{n-1} e^{-r/na_0} \ . \tag{2}$$

Figure 4 shows a surface of equal probability density (50% of the maximum value) for $n = 50$. This surface defines a torus centred on a circular orbit, in the plane perpendicular to the quantization axis Oz. This orbital is indeed the atomic level closest to the circular orbits of the century-old Bohr model.

The relative dispersion of r, $\Delta r/r$, and the fluctuation of θ, $\Delta\theta$, are equal:

$$\Delta r/r = \Delta\theta \approx 1/\sqrt{2n} \ . \tag{3}$$

The higher the level, the tighter is the confinement around the Bohr orbit. This wave function provides a representation of the electron state as close as it can get to a classical description. The phase of the orbital motion remains completely undetermined and the electron delocalized along the orbit. The azimuthal localization of the electron is precluded by Heisenberg uncertainty relations.

The analogy with the classical orbit goes beyond this simple geometrical property. Since all quantum numbers are large, most features of circular Rydberg atoms

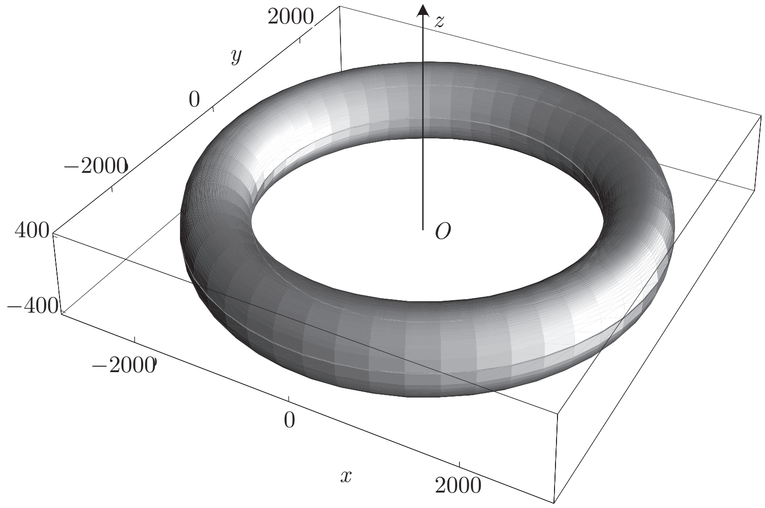

Figure 4: Surface of equal value (50% of the maximum value) for the spatial probability distribution of the valence electron in $|g\rangle = |50C\rangle$. The dimensions are in units of the Bohr radius, a_0.

can be explained by classical arguments, as stated by the correspondence principle, another major contribution of Bohr to the development of quantum physics.

As a first example, let us consider the angular frequency $\omega_{nC,(n-1)C}$ of the transition between neighbouring circular states $|nC\rangle$ and $|(n-1)C\rangle$. It is, to the first non-vanishing order in $1/n$, obtained by differentiating the binding energy with respect to n:

$$\omega_{nC,(n-1)C} \approx 2\frac{R}{\hbar}\frac{1}{n^3} \ . \tag{4}$$

The corresponding frequency is 51.099 GHz for the $|e\rangle \to |g\rangle$ transition. In a classical picture, this is the frequency of the orbital motion of the electron in a Bohr orbit. The n^{-3} dependence of $\omega_{nC,(n-1)C}$ can be interpreted in classical terms, by invoking Kepler's third law, which applies to all orbital motions in $1/r$ potentials. The period $2\pi/\omega_{nC,(n-1)C}$ of the electron must scale as the $3/2$ power of the orbit radius $a_0 n^2$. The relation between the Rydberg transition frequencies and the circular state sizes could thus have been derived by Kepler or Newton without any quantum consideration!

This simple analysis does not account for the fine or hyperfine structure contributions to the electron energy. These effects are very small in circular states. The fine structure, due to relativistic corrections including spin–orbit coupling, scales as $1/n^5$. It is only a few hundred Hertz for $n = 50$. Hyperfine structures due to magnetic couplings between the atomic nucleus and the valence electron are three orders of magnitude smaller.

The $|nC\rangle \to |(n-1)C\rangle$ transition is σ^+-circularly polarized. Its dipole matrix element d is:

$$d = a_0|q|n^2/\sqrt{2} \ , \tag{5}$$

where $|q|$ is the absolute value of the electron charge. This dipole is extremely large, 1770 atomic units for the $|e\rangle \to |g\rangle$ transition.

In the absence of external fields, the circular state is degenerate with a large number of non-circular levels having the same n and smaller ℓ and m values. A small

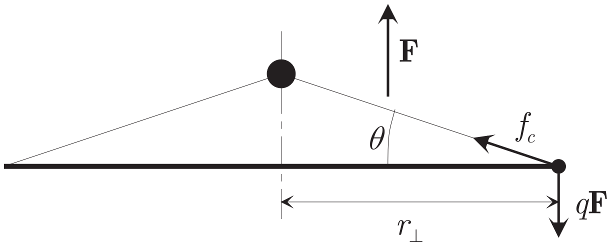

Figure 5: Classical Bohr orbit in an electric field. The field is vertical and the orbit is seen from the side, appearing as a thick line. The large black dot represents the ionic core.

perturbing electric or magnetic field, transverse to the Oz axis, would efficiently couple the circular state to the levels with $\ell = n - 2$, which would in turn be coupled to other levels with lower angular momentum. The circular orbit would be rapidly lost, the atom evolving into an uncontrolled superposition of non-circular states [26]. A perfect cancellation of the stray fields is impossible in practice, but the circular orbit can be 'protected' by subjecting the atom to a directing electric field, aligned with Oz. This field lifts the degeneracy between the circular level and the levels with $\ell = n - 2$. If it is much larger than the stray fields, the perturbing transitions are suppressed. This field, as we will see, leads to severe constraints for the microwave cavity design.

The circular state energy is shifted to second order by the directing field. This Stark shift is convenient to tune the atomic transition frequency, a procedure used in many of our experiments. A classical argument leads again to the electric polarizability of the circular state. Figure 5 shows a circular Bohr orbit – seen from the side as a straight line – normal to the applied electric field $\mathbf{F}$. The force produced on the electron, $q\mathbf{F}$, adds to the Coulomb force of the core, $\mathbf{f}_c$. The orbit remains circular (due to symmetry), but the core pops out of the orbit's plane, producing an induced electric dipole. Let us call θ the angle between $\mathbf{f}_c$ and the orbit plane and $r_\perp$ the radius of the perturbed orbit. When the external field is applied, the electron angular momentum, $m_0\omega r_\perp^2$ (m_0: electron's mass) remains constant, equal to $(n-1)\hbar \approx n\hbar$, since no torque is produced by $q\mathbf{F}$. The electron orbital angular frequency ω and orbit radius $r_\perp$, both affected by the electric field, remain linked by:

$$\omega \approx \frac{n\hbar}{m_0 r_\perp^2} \ . \tag{6}$$

The core-to-electron distance is larger than $r_\perp$ by the factor $1/\cos\theta$. The atomic Coulomb force $\mathbf{f}_c$ thus scales as $\cos^2\theta/(r_\perp)^2$ and its component along the vertical direction as $\cos^2\theta\,\sin\theta/(r_\perp)^2$. Let us project Newton's equation for the electron motion onto the electric field axis and express the balance between the force induced by the external field and the Coulomb force along this axis:

$$\cos^2\theta\sin\theta = \left(\frac{r_\perp}{a_0}\right)^2 \frac{F}{F_0} \ , \tag{7}$$

where:

$$F_0 = |q|/4\pi\varepsilon_0 a_0^2 = 5.14\,10^{11}\ \text{V/m} \ , \tag{8}$$

is the atomic electric field unit. In the orbit plane, the projection of the Coulomb force, proportional to $\cos^3\theta/(r_\perp)^2$, balances the centrifugal force, $m_0\omega^2 r_\perp$. Eliminating ω, we get:

$$\cos^3\theta = a_0 n^2/r_\perp \ . \tag{9}$$

In the weak field limit ($F \ll F_0, \theta \ll 1$), the variation of the orbit radius is negligible: $r_\perp \approx a_0 n^2$. By a first order expansion, we obtain the induced dipole d_i:

$$d_i = a_0|q|n^6 F/F_0 \ , \tag{10}$$

proportional to the applied field. The atomic polarizability scales as the sixth power of the principal quantum number. The polarization energy, E_2, is computed by considering a process in which the dipole is built adiabatically in a field increasing from zero to its final value F. Adding the elementary works done on the electric charges as the field is increased, we get $E_2 = -d_i F/2$. The second-order energy shift is finally:

$$E_2 = -Rn^6(F/F_0)^2 \ . \tag{11}$$

This expression of the Stark shift agrees with the quantum calculation, in the asymptotic limit of a large n. For $n = 50$, the level shift is -1.8 MHz/(V/cm)^2. The differential shift of the $|e\rangle \rightarrow |g\rangle$ transition is ≈ -250 kHz/(V/cm)^2.

In the high-field limit, the variation of the orbit's radius cannot be neglected. Eliminating $r_\perp$, we get:

$$\cos^8\theta\sin\theta = n^4 F/F_0 \ . \tag{12}$$

The left-hand side term in this equation is bounded. Its maximum value, about 0.2, is reached for $\theta = \arcsin 1/3 \approx 19°$. There is thus a maximum value of the electric field compatible with a stable orbit, corresponding to an ionization threshold $F_i \approx 0.2F_0/n^4$. The predicted values for $|g\rangle$ and $|e\rangle$ are, respectively 165 and 152 V/cm, to be compared to the measured values 145 and 134 V/cm. The differences are due to the ionization by tunnel effect in a field slightly smaller than the classical ionization threshold [25]. As far as the ionization is concerned, the classical limit of correspondence principle is not yet fully reached for $n = 50$. The ionization thresholds correspond to relatively low fields, easily applied to the atoms.

The detection in D (Fig. 3) uses field ionization. The resulting electrons are detected with high efficiency, up to $90 \pm 10\%$ [27]. The rapid variation of the ionizing field with n provides a state-selective detection (the two atomic levels are ionized at different times in a ramp of electric field). The errors in the attribution of n are a few percent only.

The spontaneous emission rate Γ_n of a circular state $|nC\rangle$ can also be derived by classical arguments. The electric dipole selection rule $\Delta\ell = \pm 1$ allows a unique decay channel for this state: the microwave transition towards the lower circular state $|(n-1)C\rangle$. In a classical picture, the electron, accelerated on its circular orbit, radiates electromagnetic power proportional to the modulus square of its centripetal acceleration $\mathbf{a}$. Its mechanical energy accordingly decreases slowly, as it spirals down to the core, jumping between circular states of decreasing principal quantum numbers. The radiative lifetime of the initial state corresponds to the loss of an energy amount $\hbar\omega_{nC,(n-1)C} \approx 2R/n^3$.

The radiated power $\mathcal{P}_r$ is given by the Larmor formula [28]:

$$\mathcal{P}_r = \frac{q^2 a^2}{6\pi\varepsilon_0 c^3} \ , \tag{13}$$

and the spontaneous emission rate is thus:

$$\Gamma_n = \frac{n^3 \mathcal{P}_r}{2R} \ . \tag{14}$$

Writing the electron acceleration as:

$$a = |\mathbf{a}| = \frac{1}{m_0} \frac{q^2}{4\pi\varepsilon_0 (a_0 n^2)^2} = \frac{1}{m_0 n^4} \frac{2R}{a_0} \ , \tag{15}$$

and replacing R by its expression $q^2/(8\pi\varepsilon_0 a_0)$, we obtain:

$$\Gamma_n = 2R \frac{q^2}{6\pi\varepsilon_0 c^3} \frac{1}{m_0^2 a_0^2} n^{-5} \ . \tag{16}$$

Writing a_0 as $4\pi\varepsilon_0\hbar^2/(m_0 q^2)$, we can factorize the cube of the fine structure constant α and get:

$$\Gamma_n = \frac{1}{T_{a,n}} = \frac{4}{3}\frac{R}{\hbar}\alpha^3 n^{-5} \ , \tag{17}$$

which coincides, for large ns with the expression derived from a Fermi Golden rule argument in a quantum description of the spontaneous emission process. We can finally express Γ_n in terms of the electron frequency $\omega_{nC,(n-1)C}$ as:

$$\frac{\Gamma_n}{\omega_{nC,(n-1)C}} = \tfrac{2}{3}\alpha^3 n^{-2} = 1/Q_{a,n} \ . \tag{18}$$

The inverse of this very small dimensionless ratio defines the radiative quality factor $Q_n = 3n^2/2\alpha^3$ of the circular to circular state transition. The large $\alpha^{-3} = 137^3$ factor entails that usual excited atomic excited states (n small) decay slowly at the atomic time scale, with radiative damping times corresponding typically to $3 \cdot 10^6$ periods of the emitted field. This radiative quality factor is, in circular Rydberg states, increased by a factor of n^2. For $n \approx 50$, the decay takes $\sim 10^{10}$ periods of the emitted microwave. More precisely, $\Gamma_{51} = 28$ s^{-1}, corresponding to a lifetime for $|e\rangle$ of 36 ms and to $Q_n = 1.14\,10^{10}$.

In spite of their extremely strong coupling to the millimetre-wave field, the circular Rydberg atoms are very stable. Among all possible bound orbits, the circular ones have the smallest average acceleration, the electron always remaining far from the core. The radiation loss is minimum, hence the advantage of using circular Rydberg atoms for CQED physics. Elliptical orbits (low ℓ quantum states) have a much shorter lifetime, proportional to n^{-3} instead of n^{-5}, due to the stronger acceleration of the electron near the core.

Circular atoms can travel over a few metres at thermal velocity within their lifetime. Spontaneous emission is thus negligible in an experimental set-up whose size is a few tens of centimetres. In the presence of a thermal field with $n_{\rm th}$ photons per mode on the average, the lifetime is reduced by a factor $1+n_{\rm th}$. It is thus essential to screen efficiently the room-temperature blackbody field, corresponding to tens to hundreds of photons per mode in the millimetre-wave domain. In our experiments, the circular Rydberg atoms propagate in a cryogenic environment cooled down to 0.8 K.

Circular states, with their long lifetimes, simple structure and extremely strong coupling to the field are clearly the closest to the Bohr's model orbit. More importantly, they are almost ideal tools for cavity QED experiments. However, they cannot be simply excited from the atomic ground state using only lasers. A two-step process needs to be implemented [24, 29]. A laser excitation first provides a large energy to the atom and brings it into a low angular momentum Rydberg level. The atom is then fed with a large number of radio-frequency photons, each adding one unit of angular momentum, with a very small amount of energy. The process is similar to a controlled change of orbit for a satellite, using successive rocket boosts. The details of the method are rather complex. They are described in some details in [10, 30]. We achieve the preparation of $|e\rangle$ or $|g\rangle$ with purity better than 98%.

This preparation occurs at a well-defined time (the initial laser pulse duration is 2 μs typically). It operates on a pulsed velocity-selected atomic beam. The time of flight selection between the pulsed velocity-selective optical pumping and the pulsed excitation to the Rydberg levels provide a selection of the velocity with a ±1 m/s accuracy. The position of the atomic sample is thus well known at any time during its $\approx$40 cm travel through the apparatus. It is thus possible to address it selectively along its path, for instance in the Ramsey cavities R_1 and R_2.

The weak laser excitation of the atomic beam produces Poissonian statistics for number of atoms in circular states. Due to the finite detection efficiency, it is not possible to rely on exact atom counting at detection time. We must choose instead to prepare in a sample much less than one atom on the average (typically 0.1). When an atom is counted, the probability that an undetected second atom is present is small ($< 10\%$).

This post-selection of single-atom events is obtained at the expense of a considerable lengthening of the data acquisition time. This is of course a strong limitation when it comes to performing predetermined complex sequences of quantum information processing [31]. It is, as we will see in the next Section, not a serious problem in using the atoms for a Quantum Non Demolition measurement of the field intensity.

2.2 Superconducting millimetre-wave cavities

The circular Rydberg states are stable only in a static directing electric field. It is thus impossible to use a closed superconducting millimetre-wave cavity. We have to use an open Fabry-Perot, made up of two mirrors facing each other, across which a static field can easily be applied. The photon (or classical energy) storage time, T_c, is the most critical parameter in these experiments. A long T_c requires a very high mirror conductivity, which can only be provided by superconducting metals at cryogenic temperatures. It also requires an excellent surface state to minimize losses induced by diffraction on defects.

The quest for high-quality cavities has been a long process, since these two requirements are somewhat incompatible. We finally developed a fabrication technique based on diamond-machined copper substrates, with an extremely smooth surface (10 nm roughness), covered with a thin (12 μm) layer of high-purity Niobium deposited by cathode sputtering [32].

The mirrors have a 50 mm radius and are $L = 27$ mm apart. They have a toroidal shape in order to lift the polarization degeneracy. They sustain a non-degenerate TEM_{900} Gaussian mode with a linear polarization orthogonal to the cavity axis and a waist $w = 6$ mm. The frequency of the mode is adjusted by piezoelectric elements changing the cavity length. The damping times of the cavities used in recent experiments range from 65 ms to 0.13 s, a macroscopic time interval. The latter corresponds to a quality factor $Q = 4.5\,10^{10}$ and to a finesse $\mathcal{F} = 4.9\,10^{9}$, a thousand times larger than that of the best optical cavities.

2.2.1 A harmonic oscillator

The mode is a quantum harmonic oscillator, with the Hamiltonian $H_c = \hbar\omega_c(N + 1/2)$, where ω_c is the field's angular frequency and $N = a^\dagger a$ is the photon number operator (a is the photon annihilation operator). The eigenstates of H_c are the non-classical Fock states $|n\rangle$, with a well-defined number n of photons, whose energy is $\hbar\omega_c(n+\frac{1}{2})$. The ground state is the vacuum $|0\rangle$. The Fock states are an orthogonal set:

$$\langle n\,|p\rangle = \delta_{np}\ . \tag{19}$$

The photon annihilation and creation operators a and $a^\dagger$ connect the Fock states:

$$a\,|n\rangle = \sqrt{n}\,|n-1\rangle\ \ ; \qquad a^\dagger\,|n\rangle = \sqrt{n+1}\,|n+1\rangle\ \ . \tag{20}$$

The action of a on $|0\rangle$ gives a null vector (it is not possible to annihilate a photon in vacuum). All Fock states can be generated from the vacuum by repeated applications of the photon creation operator: $|n\rangle = a^{\dagger n}\,|0\rangle/\sqrt{n!}$. Creation and annihilation operators obey a bosonic commutation rule: $\left[a, a^\dagger\right] = \mathbb{1}$.

The cavity mode electric field operator at position $\mathbf{r}$ writes:

$$\mathbf{E}_c = i\mathcal{E}_0\left[\mathbf{f}(\mathbf{r})a - \mathbf{f}^*(\mathbf{r})a^\dagger\right]\ . \tag{21}$$

The dimensionless vector function $\mathbf{f}(\mathbf{r}) = \boldsymbol{\epsilon}_c f(\mathbf{r})$ describes the spatial structure of the field mode (relative field amplitude f and polarization $\boldsymbol{\epsilon}_c$). At the geometric centre of the cavity, which we also take as the origin, the field mode amplitude is maximum and $f = 1$. The 'field per photon' $\mathcal{E}_0$ is:

$$\mathcal{E}_0 = \sqrt{\frac{\hbar\omega_c}{2\varepsilon_0\mathcal{V}}} = 1.5\,10^{-3}\ \text{V/cm}\ , \tag{22}$$

where the cavity mode volume $\mathcal{V}$ is:

$$\mathcal{V} = \int |\mathbf{f}(\mathbf{r})|^2\,dV = \frac{\pi w^2 L}{4}\ . \tag{23}$$

The field quadrature operators correspond to a mechanical oscillator's position and momentum:

$$X = \frac{a+a^\dagger}{2}\quad ;\quad P = \frac{a-a^\dagger}{2i}\ , \tag{24}$$

with the eigenstates $|x\rangle$ and $|p\rangle$ ($X\,|x\rangle = x\,|x\rangle$; $P\,|p\rangle = p\,|p\rangle$). They satisfy the commutation rule $[X, P] = i/2$, which correspond to the uncertainty relation$\Delta X\Delta P \geq 1/4$. The expectation values $\langle n|\,X\,|n\rangle$ and $\langle n|\,P\,|n\rangle$ of the field quadratures in a Fock state is zero. There is no preferred phase neither in the vacuum nor in any Fock state, a feature which shows that these quantum states are quite different from classical fields.

2.2.2 Coherent states

The classical source S (Fig. 3), weakly coupled to the mode via the diffraction loss channels, can be used to inject in C a coherent semi-classical state $|\alpha\rangle$ defined by the complex amplitude α. This injection is represented by the unitary displacement operator $D(\alpha) = \exp\left(\alpha a^\dagger - \alpha^* a\right)$, with $|\alpha\rangle = D(\alpha)\,|0\rangle$. The coherent state is an eigenstate of the annihilation operator a (with eigenvalue α). It follows that the average values of the quadratures X and P are simply the real and imaginary parts of the complex amplitude α and that their quantum fluctuations are the same as in the vacuum state. Pictorially, the coherent states can be represented in the complex amplitude plane (Fresnel plane) as a small disk of radius unity (representing the size of the quantum fluctuations) centred on the classical amplitude α.

For very small fields (about one photon on the average) the complex amplitude α is comparable to these uncertainties and quantum fluctuations play an important role. For very large amplitudes, quantum fluctuations are negligible and the coherent state can be viewed as a classical object, with well defined phase and amplitude. Coherent states stored in a cavity thus span the quantum to classical transition, with the mere adjustment of the source controls.

The coherent states can be expanded on the Fock states basis as $|\alpha\rangle = \sum_n c_n\,|n\rangle$ with $c_n = \exp(-|\alpha|^2/2)\alpha^n/\sqrt{n!}$. Their photon number distribution, $P(n) = |c_n|^2$, is Poissonian with an average $\overline{n} = |\alpha|^2$. The square modulus of the scalar product of two coherent states is thus:

$$|\langle\alpha \mid \beta\rangle|^2 = e^{-|\alpha-\beta|^2}\ . \tag{25}$$

The overlap of two such states decreases exponentially with their 'distance' in phase space. Although they are never strictly orthogonal, they become practically so when the distance of their amplitudes is much larger than 1, the radius of the uncertainty circle.

Note that the displacement operator describes a global translation in phase space. In particular, it acts on an initial coherent state $|\beta\rangle$ according to $D(\alpha)\,|\beta\rangle = \exp(\alpha\beta^* - \beta\alpha^*)\,|\beta+\alpha\rangle$, a quantum version of the addition of classical fields in the Fresnel plane.

The coherent states have a simple time evolution. Starting from $|\alpha\rangle$ at time 0, we are at time t in the state:

$$|\Psi(t)\rangle = e^{-i\omega_c t/2}\left|\alpha e^{-i\omega_c t}\right\rangle\ . \tag{26}$$

Besides a trivial phase factor (that could be removed by subtracting the constant vacuum energy from the cavity mode Hamiltonian), the coherent state amplitude evolves exactly as its classical counterpart. Accordingly, the average values of the quadratures X and P oscillate at the angular frequency ω_c, as the position and momentum of a classical oscillator.

2.2.3 Cat states

We give here a special attention to superpositions of two quasi-orthogonal coherent states, represented in the Fresnel plane by two non-overlapping circles. These states are quantum superpositions of fields with different classical properties. They are thus quite reminiscent of the Schrödinger cat thought experiment [9]. We will see later how these exotic states can be prepared in an experiment illustrating Bohr's complementarity and used to study the dynamics of decoherence. As a simple example, we consider a linear superposition with equal weights of two coherent states with opposite phases. This superposition, called a π-phase cat in the following, writes:

$$|\Psi_{\rm cat}^{\rm even}\rangle = \frac{|\beta\rangle + |-\beta\rangle}{\sqrt{2\left(1+e^{-2|\beta|^2}\right)}} \approx (1/\sqrt{2})\left(|\beta\rangle + |-\beta\rangle\right) \ , \tag{27}$$

where β is the amplitude of the field (taken real). The denominator in the first r.h.s. term is a normalization factor, taking into account the overlap of $|\beta\rangle$ and $|-\beta\rangle$. If $|\beta| \gg 1$, this overlap is negligible and the cat state is expressed by the simpler form given by the second r.h.s. term.

The coherence between the two components of the cat state is revealed by considering its photon number distribution. The state $|\Psi_{\rm cat}^{\rm even}\rangle$ develops only along even number states, since the probability for finding n photons in it is proportional to $1+(-1)^n$, justifying the superscript 'even' in its name. Similarly the cat state:

$$|\psi^{\rm odd}\rangle = (1/\sqrt{2})[|\beta\rangle - |-\beta\rangle] \ , \tag{28}$$

develops only along the odd photon numbers. We call it an 'odd phase cat'. The periodicity of the photon number is related to the coherence of the state, since a statistical mixture of $|\beta\rangle$ and $|-\beta\rangle$ contains all photon numbers. The modulated photon number distribution is a signature of the even and odd cats coherence.

It is hence convenient to introduce the photon number parity operator $\mathcal{P}$ [33] which admits as eigenstates all the superpositions of even photon numbers with the eigenvalue $+1$ and all the superpositions of odd photon number states with the eigenvalue 1:

$$\mathcal{P} = e^{i\pi a^\dagger a} \ . \tag{29}$$

The odd and even phase cats $|\beta\rangle \pm |-\beta\rangle$ are eigenstates of $\mathcal{P}$ with the $+1$ and -1 eigenvalues. The action of the annihilation operator on an even (odd) phase cat results in the switching of the cat parity:

$$a[|\beta\rangle \pm |-\beta\rangle] = \beta[|\beta\rangle \mp |-\beta\rangle] \ . \tag{30}$$

2.2.4 Field relaxation

The atom-cavity effective interaction time is at most in the 100 μs range, since the atoms are crossing the $w = 6$ mm cavity mode waist at thermal velocities. This is much shorter than the lifetime of the atomic levels (30 ms). Atomic relaxation can be safely neglected in our experiments, and cavity damping is the main source of decoherence.

The damping of a cavity mode, of a spring, has been described since the early days of quantum relaxation theory [34]. When C is coupled linearly to a large environment, including many degrees of freedom, whose eigenfrequencies span continuously a large interval around ω_c, the master equation ruling the evolution of the field density operator, ρ, can be cast in the general Lindblad [35] form:

$$\frac{d\rho}{dt} = \frac{1}{i\hbar}[H_c,\rho] + \sum_{i=1}^{2}\left[L_i\rho L_i^\dagger - \frac{1}{2}\left(L_i^\dagger L_i\rho + \rho L_i^\dagger L_i\right)\right] \ . \tag{31}$$

The operators L_i are simply $L_1 = \sqrt{\kappa(1+n_{th})}\,a$ and $L_2 = \sqrt{\kappa n_{th}}\,a^\dagger$, where $\kappa = 1/T_c = \omega_c/Q$ is the cavity energy damping rate and $n_{th} = 1/[\exp(\hbar\omega_c/k_BT)-1]$ the mean number of blackbody photons per mode at the mirrors temperature T, as given by Planck's law (k_B is the Boltzmann constant). Note that L_2 vanishes at zero temperature. In our experiment, $T = 0.8$ K and $n_{th} = 0.05$. The L_1 and L_2 operators, proportional to a and $a^\dagger$ respectively, describe the modifications, the 'quantum jumps' of the cavity state when a photon leaks out from the cavity into the environment or when a thermal photon is created.

Coherent states being eigenstates of the annihilation operator, they do not change when a photon escapes into the environment. They are thus rather immune to relaxation. A direct resolution of Eq. (31) at zero temperature shows that an initial coherent state $|\alpha_0\rangle$ remains coherent, its amplitude being exponentially damped with the time constant $T_c/2$. The average photon number decays thus as the classical field energy, with the time constant T_c. This feature qualifies the coherent states as (approximate) 'pointer states' for the cavity-environment coupling, according to the definition by Zurek [36].

For the photon number distribution $P(n) = \langle n|\rho|n\rangle$, the master equation reduces to:

$$\frac{dP(n)}{dt} = \kappa(1+n_{th})(n+1)P(n+1)+\kappa n_{th}nP(n-1)-\left[\kappa(1+n_{th})n+\kappa n_{th}(n+1)\right]P(n), \tag{32}$$

whose steady-state can be obtained by a detailed balance argument. It coincides obviously with the equilibrium blackbody state. If we consider an initial Fock state $|n_0\rangle$ and the $T = 0$ K case, $P(n_0)$ is ruled at short times by:

$$\frac{dP(n_0)}{dt} = -\kappa n_0 P(n_0)\ , \tag{33}$$

showing that the lifetime of the $|n_0\rangle$ state is of the order of T_c/n_0. The larger the Fock state, the smaller its lifetime.

The Schrödinger cat state are also very sensitive to decoherence. We can easily understand this sensitivity qualitatively. A cat state changes parity when we annihilate a photon. Hence, after a time such that, on the average, one photon has been lost, the parity of the cat is undetermined, and the cavity contains even and odd photon numbers at the same time. This corresponds to a statistical mixture of two coherent states, instead of a quantum superposition. The decoherence time scale is thus of the order of $T_c/\overline{n}$, where $\overline{n}$ is the average number of photons in the initial cat.

The Fock state fragility is closely related to that of the cat states. In fact, any Fock state with a large n_0 can be expressed as a superposition of n_0 non-overlapping coherent components with the same average energy. Each coherent component is rather immune to decoherence, but their quantum superposition is a fragile cat state.

2.2.5 Pictorial representations of field states

We used so far very qualitative phase space depictions of the field states. These pictures are made fully quantitative by associating unambiguously to the field state real quasi-probability distributions in the phase plane. We discuss here only the most useful, the Wigner function. It gives a vivid description of the state.

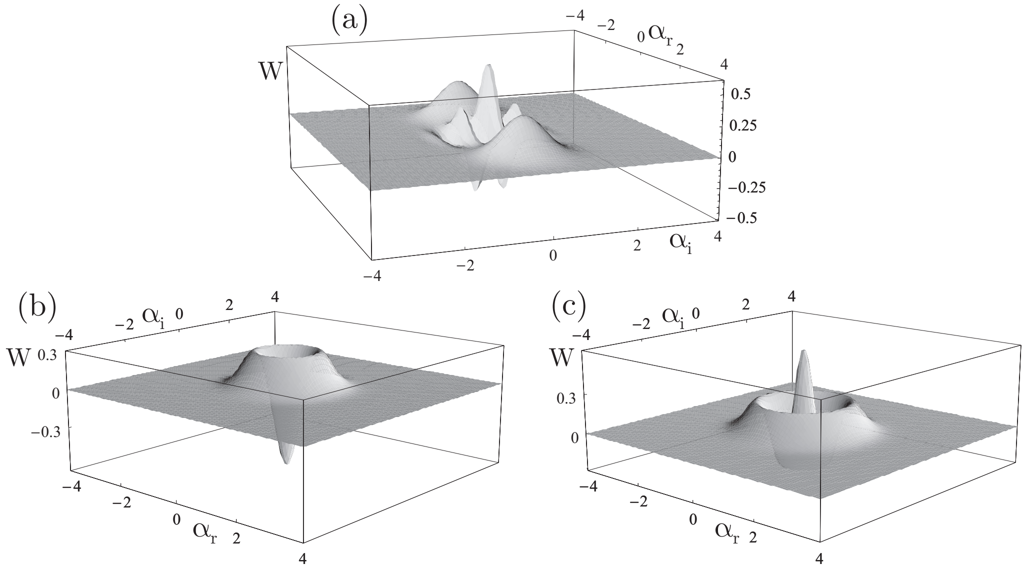

Figure 6: Plot of W functions. (a) Schrödinger cat, superposition of two 5-photon coherent states with opposite phases. (b) One-photon Fock state. (c) Two-photon Fock state.

The field is described by the density operator ρ. The Wigner distribution $W(\alpha) = W(x + ip)$ [37] is defined by:

$$W(x,p) = \frac{1}{\pi}\int dx' e^{-2ix'p}\langle x + \frac{x'}{2}|\rho|x - \frac{x'}{2}\rangle \ . \qquad (34)$$

It is the Fourier transform of an off-diagonal matrix element of ρ in a quadrature representation. The W function is real and normalized. It can take negative values in domains of phase space, making it clear that it is not a probability distribution. Negative values are, as shown below, a signature of non-classical states.

The W function of coherent states are Gaussian functions centred at the amplitude of the state. The W function of a π-phase cat is made up of two Gaussian peaks and a large interference pattern between these peaks with an alternance of positive and negative ridges [Fig.6(a)]. This pattern is a signature of the cat's coherence, lacking in the W function of a statistical mixture. The W function is thus quite appropriate for the study of a cat's coherence. Fig. 6(b) and (c) present the W function of the $n = 1$ and $n = 2$ Fock states which also exhibit negative parts.

By inverse Fourier transform of Eq.(34), the matrix elements of the field density operator are:

$$\langle x + \frac{x'}{2}|\rho|x - \frac{x'}{2}\rangle = \int dp e^{2ix'p} W(x,p) \ . \qquad (35)$$

The field density operator is thus fully determined by W. In particular, the probability density of the quadrature X, is:

$$\mathrm{Tr}\rho X = \int dp W(x,p) \ . \qquad (36)$$

The probability that X takes a given value x is obtained by integrating W for this x value, along all values of p. Schrödinger cats, for instance, have quadratures values occuring with 0 probability, a signature of their non-classical nature. The integral of W along the orthogonal quadrature vanishes, which is possible only if W presents alternances of positive and negative values. We thus understand that negativities of W are related to non-classicality.

We conclude by giving an alternative expression of W [38]:

$$W(x,p) = \frac{2}{\pi} Tr[D(-\alpha)\rho D(\alpha)\mathcal{P}] \ . \tag{37}$$

The Wigner distribution at α is the expectation value in the state translated by $-\alpha$ of the field parity operator. The Wigner function is thus a direclty measurable quantity.

2.3 The Jaynes and Cummings interaction

The atom-field interaction is described by the Jaynes and Cummings model [16]. Incidentally, the celebration of the centennial of the Bohr model also coincides with the fiftieth anniversary of this very important contribution to quantum optics. Proposed as an approximate model for the interaction of atoms with a laser, this model is a nearly exact description of the cavity QED situation.

The complete Hamiltonian is $H = H_a + H_c + H_{ac}$, where H_a is the atomic Hamiltonian, which can be written as

$$H_a = \frac{\hbar\omega_a}{2}\sigma_z, \tag{38}$$

where $\omega_a = \omega_{51C,50C}$ is the atomic transition angular frequency, and σ_z is the standard Pauli operator for the z axis of the Bloch sphere representing the state of the two-level atom.

The interaction term H_{ac} is, in the rotating wave approximation neglecting non-resonant terms, given by:

$$H_{ac} = -i\hbar\frac{\Omega_0}{2} f(vt)[a\sigma_+ - a^\dagger\sigma_-] \ , \tag{39}$$

where $\sigma_+ = |e\rangle\langle g|$ and $\sigma_- = |g\rangle\langle e|$ are the atomic raising and lowering operators.

The 'vacuum Rabi frequency', Ω_0, measures the strength of the atom-field coupling when the atom is located at the cavity centre, where the electric field amplitude is maximal. It is proportional to the dipole matrix element of the atomic transition and to the amplitude of a single photon field stored in the cavity. In our experiments, $\Omega_0/2\pi = 50$ kHz. The function $f(vt)$ reflects the variation of the atom-field coupling with time while the atom crosses the Gaussian mode at right angle with the cavity axis. Taking the origin of time when the atom reaches the axis, f simply writes $f(vt) = \exp(-v^2t^2/w^2)$.

The eigenstates of H, the atom-field 'dressed states' can be straightforwardly expressed in the basis of the uncoupled atom-cavity states $\{|e,n\rangle\}$ and $\{|g,n\rangle\}$, eigenstates of $H_a + H_c$ [10]. We will only consider here either exact atom-cavity resonance $\delta = \omega_a - \omega_c = 0$ or the non-resonant dispersive case $|\delta| \gg \Omega_0$.

At resonance ($\delta = 0$), the uncoupled states $\{|e,n\rangle\}$ and $\{|g,n+1\rangle\}$ have the same energy $[(n+3/2)\hbar\omega_c]$. Note that $|g,0\rangle$ is apart and is not affected by the atom-field coupling. The eigenstates of $H_a + H_c$ form a ladder of twofold degenerate multiplicities. The coupling H_{ac} lifts this degeneracy. The dressed states with $n+1$ excitations are $|\pm, n\rangle = (|e, n\rangle \pm i\,|g, n+1\rangle)/\sqrt{2}$, with energies separated at cavity centre ($f = 1$) by $\hbar\Omega_n$ where $\Omega_n = \Omega_0\sqrt{n+1}$.

An atom initially prepared in $|e\rangle$ in an n-photon Fock state corresponds to an initial quantum superposition of the two non-degenerate dressed states $|\pm, n\rangle$. The later evolution is thus a quantum Rabi oscillation between $|e, n\rangle$ and $|g, n+1\rangle$ at frequency Ω_n, the atom periodically emitting and reabsorbing a photon in C.

Note that, at most times during this evolution the atom-cavity system is in an entangled state. Quantum Rabi oscillations have been used in a variety of CQED experiments to create and engineer atom-field entanglement, culminating in the generation of a three-particle entangled state of the Greenberger, Horne and Zeilinger (GHZ) type [39], with three two-qubit quantum gate action [30, 31].

Note that the atomic motion through the mode is simply taken into account in this regime. A complete crossing of the mode at a constant velocity v is equivalent to a constant coupling at cavity centre during an effective interaction time $t_r = \sqrt{\pi}w/v$.

Far from resonance ($|\delta| \gg \Omega_0$), the dressed states nearly coincide with the uncoupled levels. Energy exchange between the atom and the field is prohibited by mere energy conservation. The only effect of the mutual interaction is a slight shift of the joint atom-cavity levels.

A simple second-order calculation shows that the atomic frequency is shifted at cavity centre ($f = 1$) in the field of an n-photon state by $\Delta\omega_a = 2(n + 1/2)s_0$, where $s_0 = \Omega_0^2/4\delta$. This energy shift includes a constant part, s_0, which corresponds to the Lamb shift of $|e\rangle$ induced by the vacuum fluctuations in C. The other part, $2ns_0$, proportional to the field intensity, is the few-photons limit of the light shifts usually observed in strong laser fields.

This quantized light-shift can be revealed by an atomic Ramsey [6] interferometry experiment. In the zone R_1 (Fig. 3) a $\pi/2$ pulse of classical microwave field produces, from the initial state $|g\rangle$, a superposition $(|e\rangle + |g\rangle)/\sqrt{2}$. The transient shift of the atomic frequency in C results in a phase shift of this superposition, by an amount $\phi_0(n + 1/2)$, where $\phi_0 = 2s_0t_d$. The effective dispersive interaction time is $t_d = \sqrt{\pi/2}(w/v)$. The phase-shift per photon, ϕ_0, can be adjusted by choosing the atomic velocity v or the atom-cavity detuning δ.

A second $\pi/2$ pulse is then applied in zone R_2. In a proper interaction representation, this pulse realizes the transformations $|g\rangle \rightarrow (|g\rangle + \exp(i\phi_r)\,|e\rangle)/\sqrt{2}$ and $|e\rangle \rightarrow (|e\rangle - \exp(-i\phi_r)\,|g\rangle)/\sqrt{2}$, where the phase ϕ_r of the Ramsey interferometer can be tuned by adjusting the relative phase of the pulses in R_1 and R_2 or by applying a transient Stark shift on the atomic transition between R_1 and R_2. The final probabilities $\pi_e(\phi_r|n)$ and $\pi_g(\phi_r|n)$ for detecting the atom in $|e\rangle$ or $|g\rangle$ conditioned to the presence of n photons in the cavity are oscillating functions of ϕ_r (Ramsey fringes):

$$\pi_e(\phi_r|n) = 1 - \pi_g(\phi_r|n) = \frac{1}{2}\left\{1 + \cos\left[\phi_r + \phi_0(n + 1/2)\right]\right\} . \tag{40}$$

The detection of an atom thus carries information on the photon number. Since this atom is unable to absorb the cavity field, this information has been acquired without modifying the photon number. We will use this remarkable property in the next Section.

As a reciprocal effect, the cavity frequency is shifted when an atom is in the mode. An atom in $|e\rangle$ at cavity centre shifts the cavity resonance by $\Delta_e\Omega_c = s_0$. An atom in $|g\rangle$ shifts it by an opposite amount $\Delta_g\Omega_c = -s_0$. This is the single-atom limit of an index of refraction effect. The non-resonant atom, unable to absorb or emit light, behaves as a piece of transparent dielectrics that modifies by its index the effective cavity length and thus its resonance frequency. With the strongly coupled circular atoms, this effect is large even though there is a single atom in the mode.

This index effect results in a global phase shift for a coherent state $|\alpha\rangle$ injected in C before the atom crosses it. The dispersive interaction realizes then the transformations

$$|e,\alpha\rangle \rightarrow \exp(-i\phi_0/2)\,|e,\exp(-i\phi_0/2)\alpha\rangle \tag{41}$$

$$|g,\alpha\rangle \rightarrow |g,\exp(+i\phi_0/2)\alpha\rangle \ . \tag{42}$$

3 The quantum jumps of light

Most actual measurements are quite far from the ideal, projective measurement described in elementary quantum physics textbooks. This is particularly true when it comes to counting the number of photons in a light field, for instance in a laser pulse. Modern photodetectors can count photons with a high reliability. However, instead of projecting the field on the Fock state corresponding to the obtained result, they cast it onto the vacuum, since all detected photons are absorbed, their energy being used to create the measurable electronic signal.

This total demolition of the light quantum state is not a requirement of quantum physics. It allows Quantum Non Demolition measurement process [40]. They are simply ideal projective measurements of an observable that is a constant of motion in the evolution ruled by the system's Hamiltonian. Repeated QND measurements thus always give the same result as the first one in the series. A sudden transition between two eigenvalues of the measured observable, a 'quantum jump', can be traced to an extra source of evolution for the system, due to relaxation for instance. Projective measurements of the photon number are obviously QND, since the photon number operator, N, is a constant of motion.

QND measurements of a light beam intensity have been realized with non-linear optical systems (for a review, see [41]). The intensity of the signal beam changes the index of a non-linear material (an atomic vapour for instance). This index of refraction modification is read out by a weak meter beam in an interferometric arrangement. Due to the weak optical non-linearities, these measurements only operate with macroscopic signal and meter beams, whose quantum fluctuations get correlated. They are not adapted for QND measurements at the single photon level.

As we have seen above, an atom, initially in a superposition of $|e\rangle$ and $|g\rangle$ carries, after interacting non-resonantly with the cavity, information about the photon number, coded in the phase of the atomic superposition. The dispersive interaction does not change the photon number. This information can thus be used for a QND determination of the photon number, to count the number of photons in the cavity without absorbing them. Moreover, we can send many atoms through the cavity during the energy lifetime. We can thus follow in real time the photon number and evidence the quantum jumps of light.

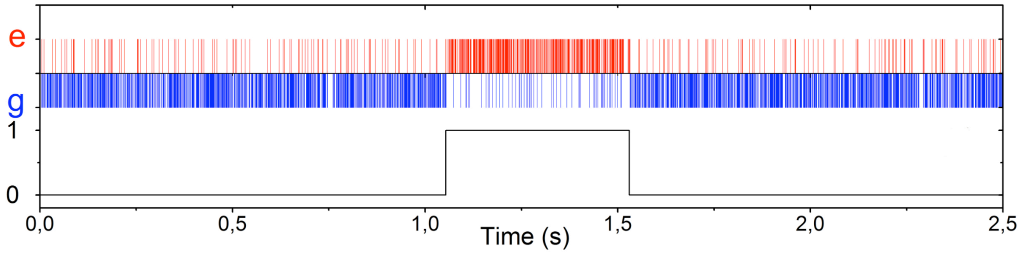

Figure 7: Monitoring the blackbody field. Top trace: atomic detections over a 2.5 s time interval. An atom found in $|e\rangle$ ($|g\rangle$) is depicted by an upwards (downwards) bar. Bottom trace: result of a majority vote over eight consecutive atomic detections revealing the birth, life an death of an exceptionnaly long-lived photon. Reprinted by permission from Macmillan Publishers Ltd: Nature [17].

3.1 Birth, life and death of individual photons

The simplest situation is when C contains either 0 or 1 photon. This is the case at thermal equilibrium. The residual blackbody field at 0.8 K contains $n_{\rm th} = 0.05$ photon on the average. Most of the time, the cavity is empty. When a thermal photon is created out of the residual fluctuations, it remains in the cavity for a time of the order of T_c. The likelihood to have two photons at the same time is extremely low.

We monitor this field by sending repeatedly atoms through the cavity [17]. The phase shift per photon ϕ_0 is set to π and the Ramsey interferometer phase ϕ_r is set so that the atom is ideally detected in $|g\rangle$ when the cavity is empty, in $|e\rangle$ when it contains a photon. The top trace in Fig. 7 presents the atomic detections observed over a 2.5 s time interval. During the first second, nearly all atoms are detected in $|g\rangle$, indicating that the cavity is empty. The few atoms detected in $|e\rangle$ are due to the finite contrast of the Ramsey interferometer. We can get rid of this residual noise by a majority vote over eight consecutive atomic detections (bottom trace).

After about 1 s, the regime changes abruptly. Nearly all atoms are now detected in $|e\rangle$. This sudden evolution reveals a quantum jump of light, the birth of a single thermal photon in the cavity. For nearly half a second, all atoms crossing the cavity agree on the presence of this photon. This is a clear indication of the Quantum Non Demolition nature of this measurement. An ordinary absorptive measurement would have resulted in the first atom after the jump exiting in the upper state $|e\rangle$. However, the photon would have been absorbed by this atom and the cavity would have been found empty by the next ones. Finally, the atoms witness the sudden death of the photon in another quantum jump and the cavity returns to its vaccum state. This particular photon has lived in the cavity for nearly 4 T_c.

This experiment is thus quite reminiscent of the famous photon box experiment of Einstein and Bohr. We are also trapping the photon in a box (if not for an infinite time) and we are weighing the box to monitor the presence of the photon. Our scale is made up of the individual Rydberg atoms crossing the cavity. The observed signals exhibit in a dramatic way the elusive quantum jumps. At the centre of the original Bohr model, quantum jumps were put in the shadow by the continuous evolution predicted by the Schrödinger unitary evolution. Many people doubted they indeed

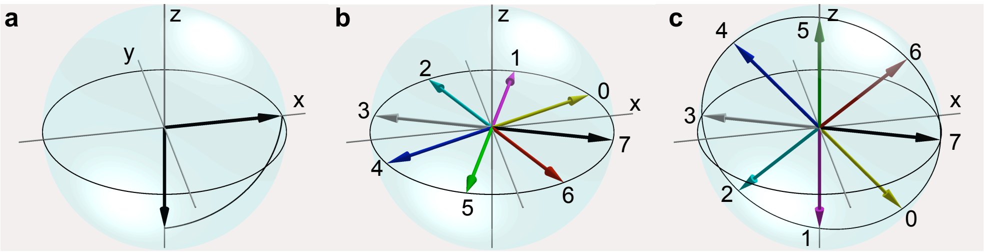

Figure 8: Evolution of the atomic Bloch vector in a QND photon-number measurement process. (a) First Ramsey $\pi/2$ pulse in R_1. (b) After the dispersive interaction with C, 8 orientations of the Bloch vector are correlated to the photon numbers from 0 to 7, for $\phi_0 = \pi/4$. (c) After the second Ramsey pulse in R_2.

were real, until they were observed for the first time on the fluorescence of a trapped ion [42, 43]. We observe them here for the first time on the light field itself. Quantum jumps are the actual evolution of a continuously monitored quantum system.

3.2 Quantum Non Demolition photon counting

The scale used in the previous Section to weigh the photon box is too sensitive to count more than one photon. The phase-shift of the atomic coherence for two photons is close to 2π and, hence, we cannot distinguish the two-photon state from the vacuum. The range of the scale can be somewhat extended. By reducing the phase-shift per photon to $\phi_0 = \pi/4$, we can count up to seven photons.

Figure 8 presents the Bloch vector describing the atomic state at successive stages in this QND process. The atom is originally prepared in $|g\rangle$ (south pole). The first Ramsey pulse in R_1 casts it in a superposition of $|e\rangle$ and $|g\rangle$ represented by a vector along the Ox axis [Fig. 8(a)]. The atom then interacts dispersively with the cavity mode, resulting in a phase shift of the atomic coherence. We have used an implicit interaction representation such that the atomic state evolution is only due to the interaction with C. After crossing the mode in the Fock state $|n\rangle$, the Bloch vector has rotated by an angle $(n + 1/2)\phi_0$.

Eight different orientations of the Bloch vector at the exit of the cavity are entangled with the photon numbers from 0 to 7 (eight photons produce the same rotation as the vacuum, $\phi_0/2$). A single atomic detection is clearly not sufficient to pin-down the photon number. After a second $\pi/2$ rotation in R_2 [Fig. 8(c)], which maps one state of the equatorial plane onto $|e\rangle$, the atom is detected in the $\{|e\rangle, |g\rangle\}$ basis, providing a single bit of information. This does not allow for a complete discrimination of the eight non-orthogonal atomic states at cavity exit. In simple terms, a single bit is not enough to count from 0 to 7!

A single atom detection realizes thus a weak measurement of the cavity field, which nevertheless changes the cavity state. Since the atom cannot emit or absorb photons, the cavity state modification is only due to its entanglement with the atom. The corresponding (completely positive) map for the field density matrix ρ is:

$$\rho \longrightarrow \rho_j = \frac{M_j \rho M_j^\dagger}{\pi_j(\phi_r|\rho)} , \tag{43}$$

where the index $j = \{e, g\}$ indicates the measured atomic state.

The measurement operators M_e and M_g are:

$$M_g = \sin\left[\frac{\phi_r + \phi_0(N + 1/2)}{2}\right] \ , \tag{44}$$

$$M_e = \cos\left[\frac{\phi_r + \phi_0(N + 1/2)}{2}\right] \ , \tag{45}$$

and define a Positive Operator Valued Measurement (POVM) with elements $E_j = M_j^\dagger M_j$, with $E_e + E_g = \mathbb{1}$. The denominator $\pi_j(\phi_r|\rho)$ in Eq.(43) is the probability for detecting the atom in state j conditioned by the field state ρ:

$$\pi_j(\phi_r|\rho) = \mathrm{Tr}\left(M_j \rho M_j^\dagger\right) \ . \tag{46}$$

Since the M_js are diagonal in the Fock state basis, this probability can also be written:

$$\pi_j(\phi_r|\rho) = \sum_n P(n)\pi_j(\phi_r|n) \ , \tag{47}$$

$P(n) = \langle n|\rho|n\rangle$ being the photon number distribution. The conditional probabilities $\pi_j(\phi_r|n)$ are given by Eq.(40).

The new photon number distribution after a detection in state j for the Ramsey interferometer setting ϕ_r, $P(n|j, \phi_r)$, is thus:

$$P(n|j, \phi_r) = \frac{\pi_j(\phi_r|n)}{\pi_j(\phi_r|\rho)} P(n) \ . \tag{48}$$

We recover here the usual Bayes law of conditional probabilities [18]. The probability for having n photons, conditioned to an atomic detection in j with the Ramsey interferometer phase set at ϕ_r is, within a normalization factor (denominator in the r.h.s.), the initial photon number distribution $P(n)$ multiplied by the conditional probability for detecting the atom in j with this Ramsey phase setting when there are n photons in the cavity. Note that if the atom escapes detection, due to the finite efficiency of D, it does not change the photon distribution, since the two density matrices corresponding to a detection in $|e\rangle$ or $|g\rangle$ should then be summed, weighted by the respective detection probabilities.

After each atomic detection, $P(n)$ is thus multiplied by a sinusoidal function of n, proportional to $\pi_j(\phi_r|n)$. Some photon numbers are less likely to be found after the measurement (those which correspond to the highest probability for detecting the atom in the other state). Sending N_a atoms one by one through C iterates this photon number 'decimation' operation. The final $P(n)$ is:

$$P_{N_a}(n) = \frac{P_0(n)}{Z} \prod_{i=1}^{N_a} \pi_{j_i}(\phi_{r,i}|n) \ , \tag{49}$$

where j_i is the detected state for the atom labelled i in the series, $\phi_{r,i}$ the Ramsey interferometer phase used for this atom and $P_0(n)$ the initial photon number distribution.

Each factor in the product on the r.h.s. decimates some photon numbers. Numerical simulations and mathematical arguments [44] show that, after many atoms have been detected, the final distribution reduces to a single photon number n_m:

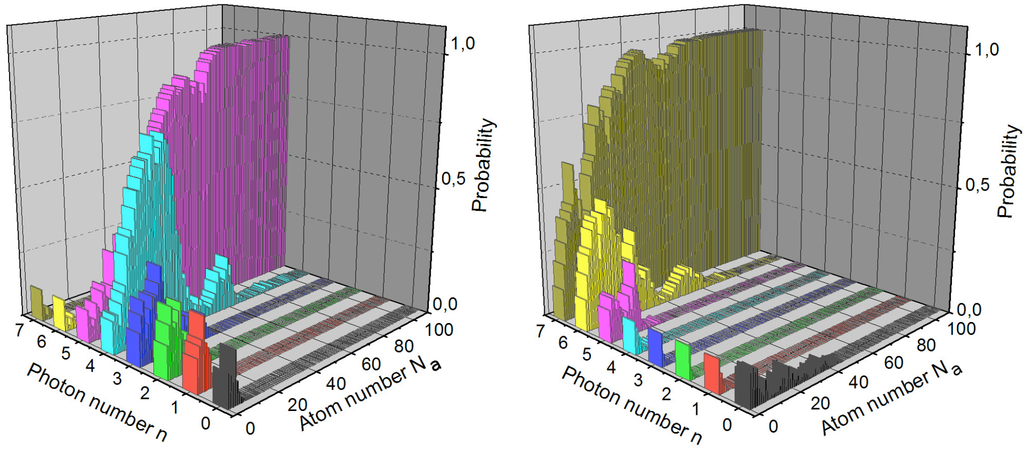

Figure 9: Two individual realizations of the QND measurement of a coherent field. The histograms show the evolution of the photon number distribution with the number N_a of detected atoms. Reprinted by permission from Macmillan Publishers Ltd: Nature [18].

$P_{N_a}(n) = \delta_{n,n_m}$, provided that the initial distribution $P_0(n)$ spans a photon number range such that no two photon numbers lead to the same detected atomic state (for instance, the $\{0,7\}$ range when $\phi_0 = \pi/4$). The accumulation of partial information provided by weak measurements ends up in a complete, projective measurement of the photon number. The final outcome is independent of the initial distribution $P_0(n)$. We can thus choose it freely, provided it does not cancel in the relevant photon number range. The logical choice is a flat distribution, reflecting our total uncertainty upon the initial cavity field before measurement.

We realized such a measurement on a coherent field with an average photon number $\overline{n} = 3.82$ (the probability for having 8 photons or more in this field is a few % only). We record the detection of $N_t = 110$ atoms, in a time of the order of 26 ms, with $\phi_0/\pi = 0.233$ rad. The Ramsey phase ϕ_r is randomly chosen among four values differing by about $\pi/4$ to speed up convergence. We use a slightly modified decimation law to incorporate the finite contrast of the Ramsey interferometer (see [18] for details).

Figure 9 presents the evolution of the photon number distribution after the detection of N_a atoms ($N_a = 0 \ldots N_t$) for two realizations of the experiment. Let us discuss that on the left. The initial $P_0(n)$ is flat. After one atomic detection, it has a sine shape. After about 20 atomic detections, the decimation process leaves only two possible photon numbers, 5 and 4. For a short time interval, 4 dominates, but, after about 70 atomic detections, only 5 is left, completing the measurement. The other realization (right part of the figure) exhibits a similar behaviour, the final photon number being then 7. We observe here the progressive collapse of the field state due to an accumulation of weak measurements.

The final photon number is selected by the random atomic detection outcomes. Each realization of the experiment leads, after recording N_t atoms, to a different, random photon number according to the basic postulates of quantum physics. "God is playing dice" in a quantum measurement. The probability for obtaining the final value n_m must be ideally given by the initial photon number distribution $P_0(n_m)$.

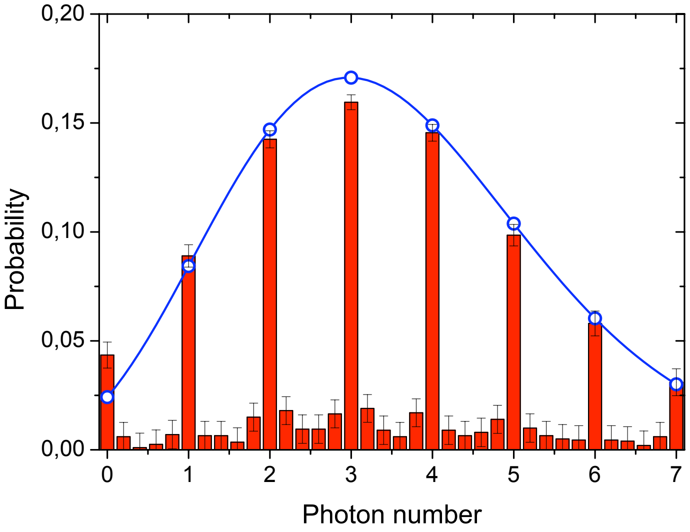

Figure 10: Reconstructed photon number distribution in the initial cavity field. Histogram of the average value $\langle n \rangle$ of the final photon distribution $P_{N_t}(n)$. The error bars reflect the statistical uncertainty (2000 realizations of the experiment have been used). The blue circles (and the continuous line joining them for visual convenience) represent a Poisson law with 3.46 photons on the average. Reprinted by permission from Macmillan Publishers Ltd: Nature [18].

We have recorded 2000 individual realizations of the detection sequence and computed, for each of them, the average photon number $\langle n \rangle$ for the final distribution $P_{N_t}(n)$. The histogram of the measured $\langle n \rangle$ values is shown in Fig. 10. In about 80% of the cases, we do finally obtain an integer photon number, showing that the decimation process has converged. The background in the histogram corresponds to 20% of the experiments for which either N_t atoms have not been sufficient to grant convergence or for which a quantum jump due to cavity relaxation occurred during the measurement process itself. When convergence is obtained, the observed probabilities fit nicely with a Poisson law (open blue circles). Its average photon number, 3.46, coincides nicely with an independent calibration of the initial cavity state.

3.3 Quantum trajectories

Since the probe atoms do not absorb the cavity field, we can follow the photon number evolution over a long time interval. We keep sending dispersive atoms in C. At each time t, we infer a photon number distribution and its average $\langle n \rangle(t)$ from information provided by the last N_t atomic detections. Figure 11(a) present the time evolution of the inferred average photon number over 0.7 s for two realizations of the experiment whose initial phases (first N_t atoms) are shown in Fig. 9.

The initial phase corresponds to the $\simeq 26$ ms time interval required to perform the state collapse. Then, we observe a plateau with a constant photon number (5 or 7). In both cases, the duration of this plateau is long enough to allow for two measurements of the photon number with two independent samples of $N_t = 110$ atoms. That these two measurements lead to the same result is a clear indication of the QND character of this process.

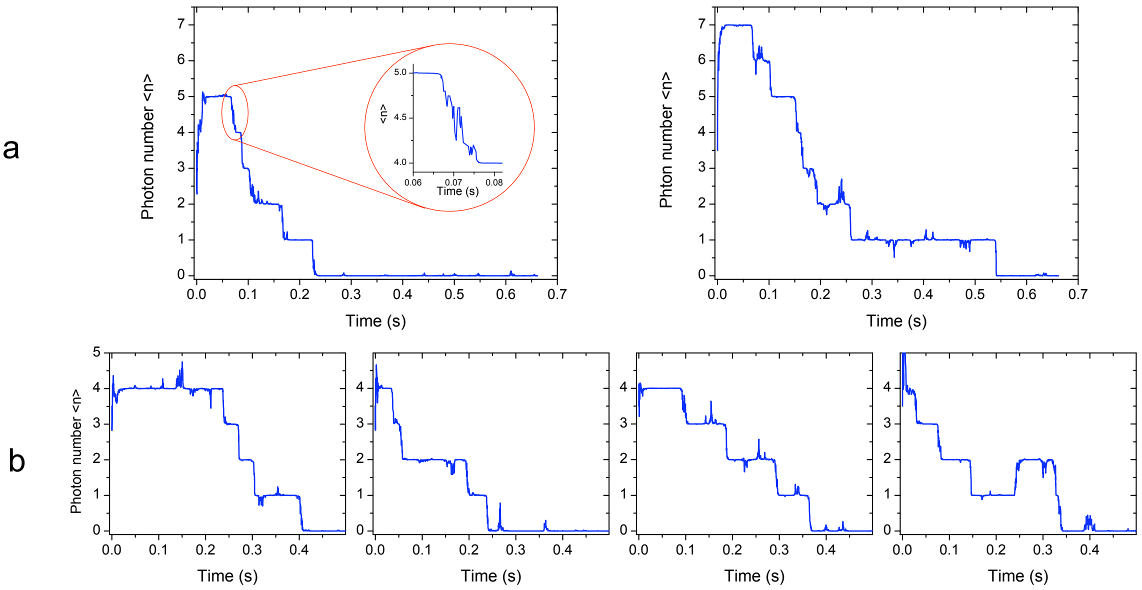

Figure 11: Repeated measurements. (a) Time evolution of the mean photon number $\langle n\rangle(t)$ for the two sequences whose collapse is shown in Fig. 9. (b) Four other trajectories with an initial collapse in the $n_m = 4$ Fock state. Reprinted by permission from Macmillan Publishers Ltd: Nature [18].

Our photon-counting procedure illustrates thus all the basic postulates for an ideal projective quantum measurement. It provides a quantized result (an integer photon number), whose value is randomly chosen with a statistical distribution given by the initial cavity state. The repeatability of the measurement shows that it does project the field state onto an eigenstate of the measured observable, the $|n_m\rangle$ Fock state, a situation radically different from that of all standard photo-detections.

After the initial plateau, we observe a stepwise relaxation of the photon number towards zero. We monitor again the quantum jumps of light, while the photons escape one by one from the cavity into the loss channels. The inset in the first curve shows a zoom on the quantum jump between the 5 and 4 photon states. Recording it requires the accumulation of information from a few tens of atomic detections and is performed in about 10 ms. Note that the one-photon state in the trajectory on the right has an exceptionally long lifetime (about 300 ms, nearly three average lifetimes T_c).

Figure 11(b) presents four other trajectories, with an initial collapse in the 4-photon state, exhibiting the randomness of the quantum jumps occurrences. Note on the rightmost trajectory an upwards quantum jump corresponding to the creation of a thermal excitation in C.

The master equation (31) predicts a smooth relaxation of the average energy, the photon number decaying exponentially with a time constant T_c. This evolution is quite different from the sudden jumps of Fig. 11. This is precisely the reason why quantum jumps were sometimes considered as impossible before their actual observation. This illustrates the difference between a single realization of a quantum experiment and the ensemble average predicted by the density operator. Averaging thousands of quantum jump trajectories, starting from randomly selected photon numbers, all exhibiting quantum jumps at different times, we indeed recover a smooth evolution in excellent agreement with the predictions of the master equation.

We have performed a detailed study of field relaxation [19]. By a careful analysis of all quantum jumps trajectories, we reconstruct the damping-induced evolution of the photon number distribution, starting from all Fock states with 0 to 7 photons. We get clear evidence of the fast decay of the high-lying Fock states, whose lifetime is T_c/n. By a fit of the complete data, we extract the coefficients of the most general linear master equation ruling the evolution of $P(n,t)$. The results of this partial quantum process tomography are in excellent agreement with Eq. (32). Similar measurements have been performed simultaneously in the context of circuit QED [45].

Finally, the QND measurement process leads naturally to the observation of the quantum Zeno effect [46]. Whereas frequently repeated measurements do not affect the dynamics of incoherent damping, they inhibit the coherent evolution of a quantum system. An observed system does not evolve under the action of its Hamiltonian, in clear correspondence with the second Zeno paradox negating motion. Quantum Zeno effect has been observed on the evolution of a variety of two-level systems, first on a trapped ion [47].

We have observed it for the coherent evolution of the cavity field under the action of the classical source S [48]. We realize a long series of identical coherent injections with a very small amplitude in the initially empty cavity. These amplitudes add up and the field is finally in a mesoscopic coherent state, whose average photon number grows quadratically with the number of injections, or with time. When we perform, between injections, QND measurements of n, we project repeatedly, with a high probability, the field back onto $|0\rangle$, since the probability for finding $n = 1$ after a single injection is low. We observe that the field energy effectively remains nearly zero, exhibiting the Zeno effect for the classical runaway process of field injection.

3.4 Quantum feedback: combating the jumps

The QND measurement procedure presented in the previous paragraph prepares Fock states of the field. These highly non-classical states can be a quite interesting quantum resource for quantum computing, quantum enabled metrology or quantum communication. However, the measurement-based preparation is a random process. We cannot predict which Fock state will be produced in one realization of the experiment. Moreover, this resource is fragile and decoherence rapidly destroys it.

If non-classical states are to be used as a resource, it would be quite interesting to prepare them on demand and to protect them from relaxation. A possible route towards this goal is quantum feedback [49, 50], which extends to the quantum realm the feedback circuits present in every complex classical system.

As in any feedback operation, a 'sensor' gets information on the system, a 'controller' estimates a proper distance between the present state of the system and the 'target' one, and drives accordingly an 'actuator', which steers the system towards the required operating point. The main difficulty quantum feedback has to face is that the measurement by the sensor changes the system's state, making quantum feedback loops more subtle than their classical counterparts.

We have realized two experiments on a continuous feedback process preparing Fock states and protecting them against decoherence [20, 21]. In both experiments, the sensors are atoms, crossing the cavity in the dispersive regime. They provide Quantum Non Demolition information about the number of photons in the cavity.

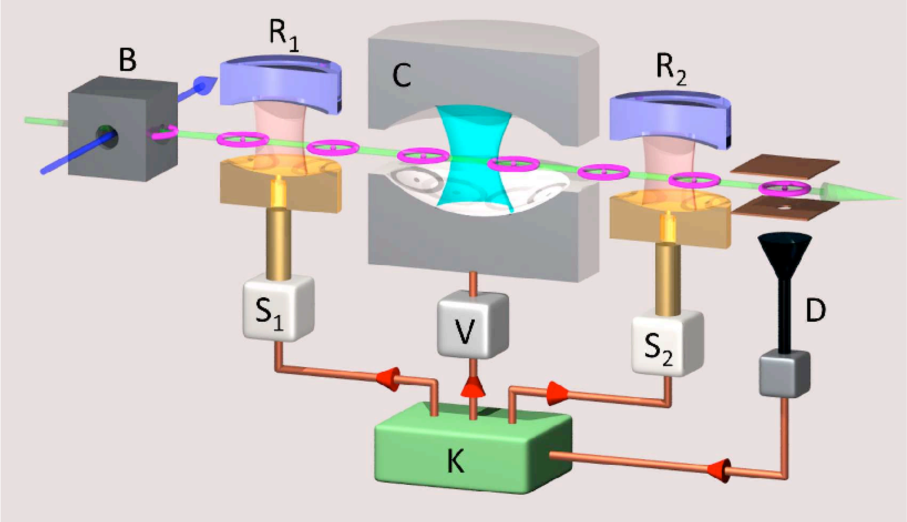

Figure 12: Principle of the quantum feedback experiment for the preparation and protection of Fock states.

This information is fed to the controller K (a fast real-time classical computer ADwin-ProII by Jäger Messtechnik). The controller performs a Bayesian estimation of the most likely state of the cavity field. It programs accordingly an actuator, which should drive the cavity as close as possible to the target Fock state $|n_t\rangle$.

The two experiments differ by the nature of the actuator. In [20], we use a classical source injecting a small coherent field in C, with controlled phase and amplitude. The interplay of these tiny displacements with the repeated measurements by the probe atoms results in the preparation and stabilization of Fock states containing up to four photons. This experiment is nevertheless limited by the nature of its actuator. A classical source is not ideal to compensate for the single photon quantum jumps due to decoherence. A quantum actuator would be much more appropriate.

In the second experiment [21], whose scheme is presented in Fig. 12, we use resonant atoms as actuators. The scheme thus implies two type of atoms. The probe atomic samples, prepared in g, undergo $\pi/2$ Ramsey pulses in R_1 and R_2 and interact dispersively with the cavity mode. The final result of their detection is fed to the controller K. The control atomic samples can be used as additional QND probes when K estimates that the cavity field is close enough to the target state. When the estimated photon number is higher than the target, K tunes these atoms at resonance with C, via the Stark shift produced by the potential V applied across the cavity mirrors. Left in the initial state g, they can thus absorb one photon out of the mode. Prepared in e by a π resonant pulse in R_1, they emit a photon in the mode. Their final state is also recorded by K, providing additional information on the feedback process. In order to get a good flux of information on the cavity state, we send repeatedly sequences made up of 12 probe samples and 4 control ones.

The main task of K is to estimate the field state after the detection of each sample, based on all available information. This estimation and the resulting actuator settings must be performed within the $T_a = 82$ μs time interval between atomic samples. Since the initial vacuum and the actuators bear no phase information, the field density matrix remains diagonal in the $\{|n\rangle\}$ basis and K needs only to update the photon number distribution $p(n)$, a considerable simplification. Moreover, the field Hilbert space is truncated to a maximum dimension of 8 and the code has been carefully optimized.

In order to get a faithful estimation of the photon number, K takes into account all the available knowledge: all atomic detections (and the measured detection efficiency in D), all actuator actions. It includes all the known and independently measured experimental imperfections, It keeps track of cavity relaxation. For the actuator atoms, K takes into account the independently measured resonant Rabi oscillations in the field of N photons. It also includes the small probability to send two resonant atoms in the same sample.

After this rather complex Bayesian inference, K obtains the estimated photon number distribution $p(n)$. It then computes all the possible photon number distributions corresponding to all choices for the next control sample at hand (which can be used as an emitter, as an absorber, or as an additional QND probe). The controller determines for each choice the expectation value of the distance to the target state $|n_t\rangle$, defined as $d = \sum_n (n - n_t)^2 p(n) = \Delta n^2 + (\overline{n} - n_t)^2$ (Δn^2 and $\overline{n}$ are the photon number variance and mean value, respectively). This distance obviously cancels only when the target is reached. The controller K finally implements for this control atom the choice leading to the smallest distance.

Figure 13 shows the data of a single realization of the experiment with $n_t = 4$. It presents, as a function of time, from top to bottom, the detected sensor states, the estimated distance d, the controller decisions to send emitter or absorber actuator samples, and finally the evolution of the photon number distribution estimated by K together with its average value. Starting from the vacuum at $t = 0$, emitting samples are repeatedly sent until d comes close to zero. The photon number distribution is then peaked on $n = n_t$, with $p(n_t) \approx 0.8 - 0.9$. Around $t = 50$ ms, a downwards quantum jump to $n = 3$ triggers the sending of few emitter samples, which rapidly restore the target state. Close to $t = 70$ ms, another downwards jump is overcorrected, leading to $n = 5$. Absorbers are then sent until restoration of the target.

The performance of the feedback procedure is assessed by reconstructing the average final photon number distribution, independently from the estimation made by K, and by comparing it to the reference Poisson distribution with n_t photons on the average shown in Fig. 14(a). The loop is interrupted at $t = 140$ ms. We then send a few QND sensor samples [18]. From 4000 realizations of this experiment, we reconstruct by a maximum likelihood procedure [19] the photon number distribution plotted in Fig. 14(b). The measured fidelities with respect to the target state, are about twice those of the corresponding Poisson distribution and the photon number distributions are clearly sub-Poissonian.

Halting a feedback loop at a randomly preset time is not the optimal way of using it. A much better performance is obtained when using the state estimation by K for interrupting the feedback at a proper time. The histograms in Fig. 14(c) present, for each n_t, the $\overline{p}(n)$ distributions obtained with 4000 sequences interrupted when K estimates that $p(n_t) > 0.8$. The obtained fidelity is close to the expected 0.8 value up to $n_t = 3$ and remains always larger than that of the histograms in Fig. 14(b).

We have implemented a real-time quantum feedback operating in the steady-state. The slow pace of the Rydberg atoms cavity QED experiments is a considerable asset, since it allows K to perform its complex state estimation procedure in the time

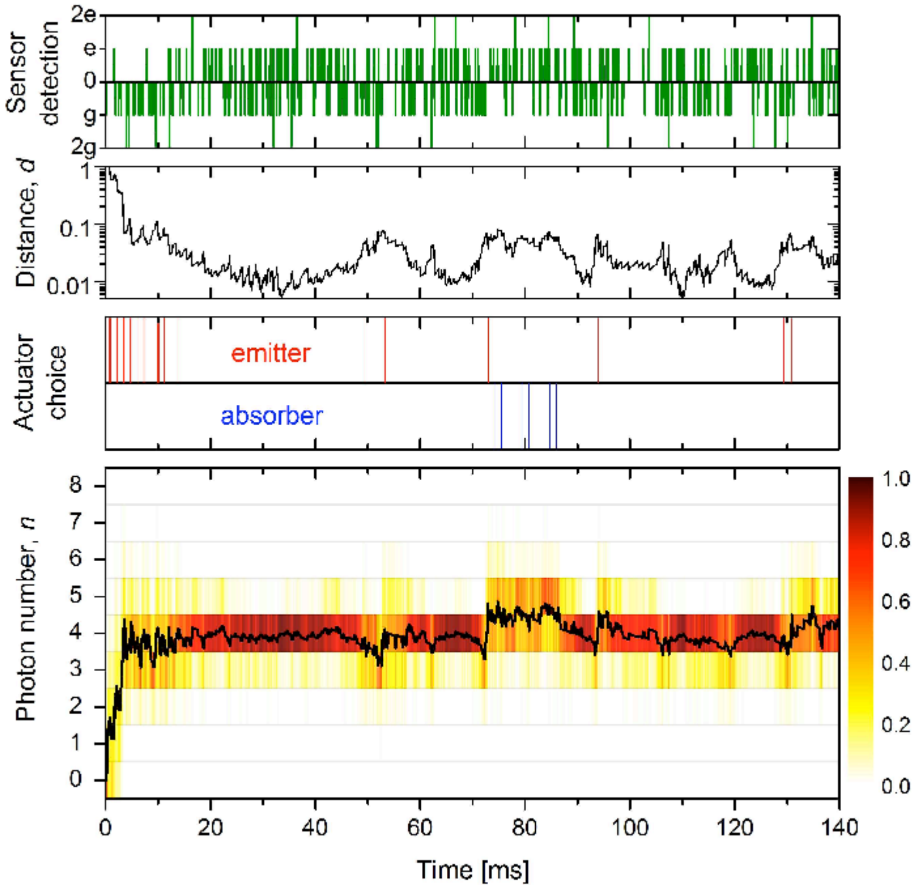

Figure 13: Single realization of the feedback experiment with $n_t = 4$. The frames present versus time, from top to bottom, the detected sensor states (upwards bars for e, downwards bars for g), the distance d to the target, the actuators sent by K (emitters or absorbers) and the photon number distribution $p(n)$ inferred by K (gray scale) together with its average value (solid black line). Reprinted by permission from Macmillan Publishers Ltd: Nature. [21].

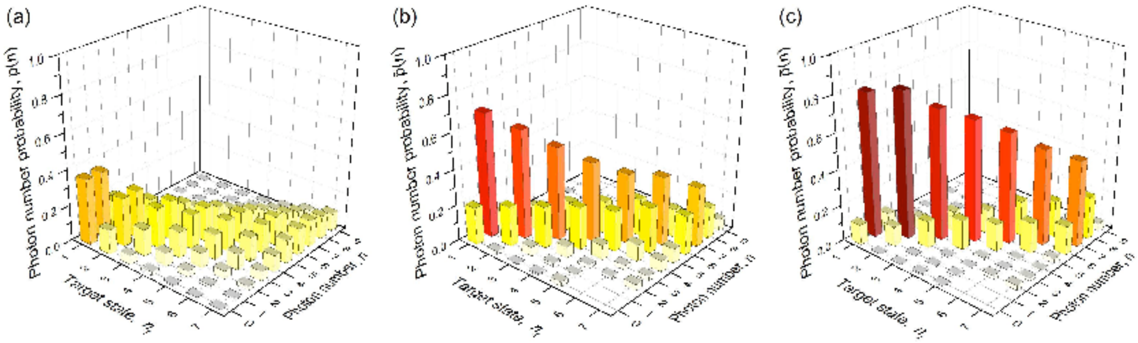

Figure 14: Histograms of photon number distribution as a function of the target photon number n_t. (a) Reference Poisson distribution with n_t photons on the average. (b) Photon number distribution measured by an independent QND process after interrupting the feedback loop at $t = 140$ ms. (c) Photon number distribution measured when K estimates that $p(n_t) > 0.8$. Reprinted by permission from Macmillan Publishers Ltd: Nature. [21].

interval between two measurements of the cavity field. This is much more difficult in optical or circuit QED experiments [51], in which the time scale is typically 1000 times faster.

4 Bohr's complementarity and the Schrödinger cat

The cavity QED set-up can also be used, in a slightly different mode, to implement another thought experiment, the Bohr's moving slit interferometer (Fig. 1). Let us consider the Ramsey interferometer made up of the zones R_1 and R_2. The oscillations with ϕ_r of the probability π_e for detecting the atom in $|e\rangle$ result from the quantum interference between two different paths. Either the atom, initially in $|g\rangle$ and finally in $|e\rangle$ absorbs a photon from the classical source in R_1 or it absorbs it in R_2. Since the classical microwave field involves many photons, the addition of a single photon in the low-Q Ramsey cavities does not modify appreciably their fields. Thus, the two paths leading from the initial to the final state are indistinguishable and the quantum interference of their probability amplitudes results in the Ramsey fringes.

When the cavity contains a Fock state, this picture is not modified. The Fock state is unchanged by an atom crossing C either in $|e\rangle$ or in $|g\rangle$. The two paths remain indistinguishable and we get Ramsey fringes, with a phase shift reflecting the transient shift of the atomic enery levels in the cavity.

4.1 Atomic interferometry and "which-path" information

Let us now focus on the case where C initially contains a coherent field $|\gamma\rangle$. As seen in Section 2.3, this coherent field is dephased in opposite directions for an atom crossing the cavity in $|e\rangle$ or in $|g\rangle$. After the atom-cavity interaction, but before the $\pi/2$ pulse in R_2 we are thus left with the intermediate entangled atom-cavity state:

$$|\Psi_i\rangle = \frac{1}{\sqrt{2}}\Big[e^{-i\phi_0/2}\,|e\rangle\,\big|\gamma e^{-i\phi_0/2}\big\rangle + |g\rangle\,\big|\gamma e^{i\phi_0/2}\big\rangle\Big]\ . \tag{50}$$

The phase of the coherent field left in the cavity thus contains which-path information about the atomic state inside the Ramsey interferometer. If this information is unambiguous, i.e. if the phase-shift ϕ_0 is much larger than the quantum uncertainty on the coherent states phase, we expect that the Ramsey fringes should disappear in direct application of the complementarity concept [2].

We can make this discussion more quantitative by writing the final atom-cavity state after R_2:

$$\begin{aligned} |\Psi_f\rangle &= \frac{1}{2}\,|g\rangle\,\left[\big|\gamma e^{i\phi_0/2}\big\rangle - e^{-i\phi_0/2}e^{-i\phi_r}\,\big|\gamma e^{-i\phi_0/2}\big\rangle\right] \\ &\quad +\frac{1}{2}\,|e\rangle\,\left[e^{i\phi_r}\,\big|\gamma e^{i\phi_0/2}\big\rangle + e^{-i\phi_0/2}\,\big|\gamma e^{-i\phi_0/2}\big\rangle\right]\ . \end{aligned} \tag{51}$$

From this state, we get the probability π_e for detecting finally the atom in $|e\rangle$:

$$\pi_e = \frac{1}{2}\Big[1 + \mathrm{Re}\,e^{-i(\phi_r+\phi_0/2)}\,\big\langle\gamma e^{i\phi_0/2}\,\big|\gamma e^{-i\phi_0/2}\big\rangle\Big]\ , \tag{52}$$

where the real part in the r.h.s. contains the Ramsey fringes signal oscillating with ϕ_r.

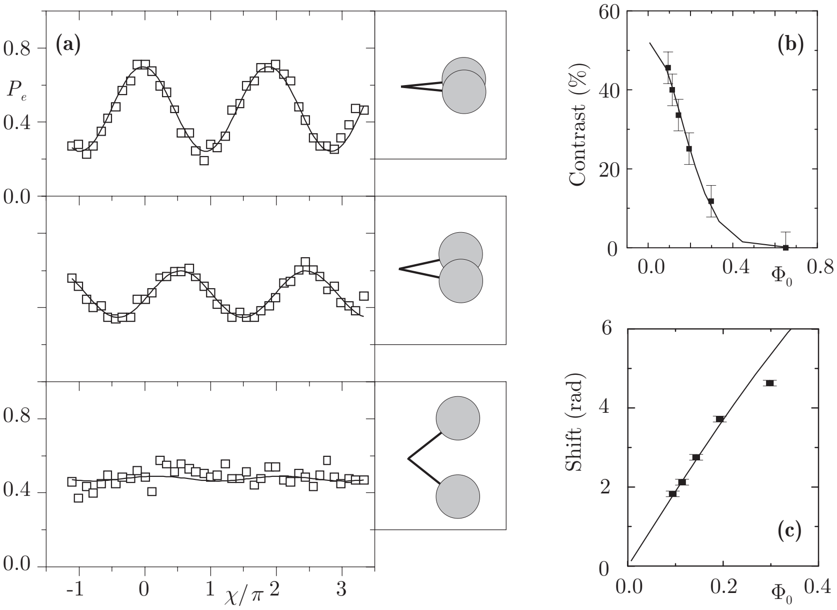

Figure 15: Schrödinger cat and complementarity. (a) Ramsey fringes for $\beta = 3.1$ and three different $\Phi_0 = \phi_0/2$ values (0.1, 0.2 and 0.69 radians, corresponding to $\delta/2\pi = 712$, 347 and 104 kHz respectively from top to bottom). The insets give a pictorial representation of the two field phase components. (b) Ramsey fringes contrast versus Φ_0. The solid line corresponds to the theoretical predictions, scaled by the finite Ramsey interferometer contrast. (c) Fringes shift (in radians) versus Φ_0. The slope of the fitted line provides a calibration of the photon number. Reprinted from [22].

When the cavity is initially empty, we obviously recover Eq. (40) for $n = 0$. When the cavity field is non-zero, the Ramsey interference signal is multiplied by the scalar product of the two coherent fields corresponding to the two quantum paths in the interferometer. We recover here in a more quantitative way our complementarity discussion. For a given phase shift per photon ϕ_0, when γ is large, the two final field states are nearly orthogonal. They record unambiguous which-path information and the interference signal is lost. When γ is small, the two field states overlap, their scalar product is nearly one and we get Ramsey fringes with a full contrast. More precisely, we can write π_e as a function of the average number of photons, $\overline{n} = |\gamma|^2$ in the initial coherent field:

$$\pi_e = \frac{1}{2}\Big[1 + e^{-\overline{n}(1-\cos\phi_0)}\cos(\phi_r + \phi_0/2 + \overline{n}\sin\phi_0)\Big] \ . \tag{53}$$

We recognise a light-shifted Ramsey signal, with a contrast decreasing exponentially with $\overline{n}$.

We have observed these Ramsey fringes with $\overline{n} = 9.5$ [22] for different phase splittings $\Phi_0 = \phi_0/2$ obtained by varying the atom-cavity detuning δ. The signals for three different values of Φ_0 are shown in Figure 15(a) with, in the insets, the final field states represented qualitatively in phase space. The collapse of the fringe amplitude when the field components separate is conspicuous. The fringe contrast is shown versus Φ_0 in Figure 15(b) and the fringe phase shift in Figure 15(c). In these plots, the points are experimental and the curves given by theory, with an overall contrast adjustment taking into account the imperfections of the Ramsey interferometer. Note that the theoretical formula above, valid in the dispersive limit, do not apply for the smallest detuning $\delta = 104$ kHz. An exact expression of the phase shifts based on the exact dressed states is used for the largest value of Φ_0. This experiment presents a direct illustration of the complementarity concept in a simple interferometer arrangement. Note that other complementarity tests, even more directly related to Bohr's moving slit original proposal have been performed with the same set-up [52].

4.2 A cat in a box

Looking into the photon box at the end of the complementarity experiment leads us to consider another thought experiment, the Schrödinger cat [9]. When the atom is finally detected, we have no information on the state in which it actually crossed the cavity, since the second $\pi/2$ pulse of the Ramsey interferometer mixes levels $|e\rangle$ and $|g\rangle$. The field must thus be left in a quantum superposition of the two phase-shifted coherent components $\left|\gamma e^{-i\phi_0/2}\right\rangle$ and $\left|\gamma e^{+i\phi_0/2}\right\rangle$, a mesoscopic quantum superpositions of two states differing by their classical phase.

More precisely, setting $\phi_r = -\phi_0/2$, a final atomic detection after R_2 projects (within an irrelevant global phase) the field onto:

$$|\Psi_\pm\rangle = \frac{1}{\mathcal{N}}\left(\left|\gamma e^{+i\phi_0/2}\right\rangle \pm \left|\gamma e^{-i\phi_0/2}\right\rangle\right) \ , \tag{54}$$

where the $+(-)$ sign applies for a detection in e (g), $\mathcal{N}$ being a normalization factor. When $\phi_0 = \pi$, we recognize the odd and even cat states introduced in Section 4. In reference to this simple situation, we call even (odd) cat the state with the $+$ $(-)$ sign for all ϕ_0 values.

The cat state is, when $|\gamma|$ is large, a quantum superposition of two quite distinct classical states. It is expected to decay rapidly due to its coupling to the environment via the cavity losses. We have performed in an early experiment [22] a first investigation of this decoherence process. It showed that the decay rate of the coherence between the superposed states increases rapidly with their separation in phase space, in good agreement with theoretical expectations.

A much more detailed insight into the cat decoherence can be obtained through a complete reconstruction of the field density operator ρ as a function of time. As discussed in Section 3.2, the QND measurement of the photon number leads to a partial reconstruction. Many measurements performed on the same quantum state allow us to reconstruct the photon number distribution, *i.e.* the diagonal of the density operator in the Fock state basis. We have no access, however, to the non-diagonal elements, which contain information on the field phase distribution. We are unable, for instance, to distinguish a statistical mixture of Fock states with no phase information from a coherent state, with a well-defined phase. Since we use non-resonant probe atoms, they cannot extract information about the field phase.

A simple modification of the QND scheme allows us to reconstruct the full density operator [23]. Before sending the QND probe atoms, we perform a displacement of the cavity field, by letting the source S inject in C a coherent amplitude β with a well defined phase with respect to the initial cavity field amplitude γ. This 'homodyning' procedure turns the cavity field density operator ρ into $\rho_\beta = D(\beta)\rho D(-\beta)$. We then send many QND probe atoms through C. By repeating the experiment many times, we measure the probability $\pi_e(\phi_r|\rho_\beta)$, conditioned

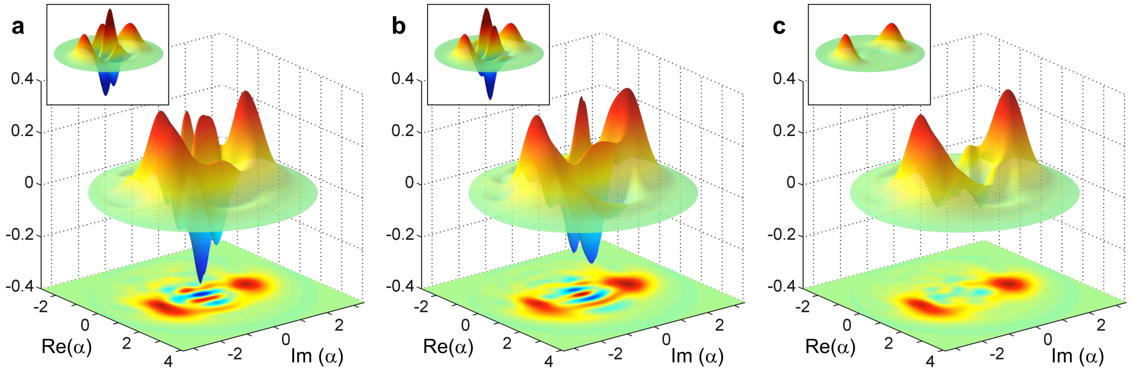

Figure 16: Experimental Wigner functions of an even cat (a), odd cat (b) and statistical mixture of two coherent components (c). The insets present the theoretical expectations. The average photon number is 3.5 and the phase shift is $\phi_0 = 0.74\pi$. Reprinted by permission from Macmillan Publishers Ltd: Nature [23].

to the translated cavity state. It writes simply $\pi_e(\phi_r|\rho_\beta) = \mathrm{Tr}\,[G(\beta,\phi_r)\rho]$, where $G(\beta,\phi_r) = D(-\beta)M_e^\dagger M_e D(\beta)$. We thus obtain finally, within statistical noise, the average of the observable $G(\beta,\phi_r)$ in the initial cavity state.

Resuming the experiment for very many (up to 600) different translation amplitudes β carefully chosen in phase space, we obtain the average value of many different observables $G(\beta,\phi_r)$ in the state ρ. We infer from these results all the matrix elements of ρ, using an approach based on the maximum entropy principle [53]. This procedure determines the density matrix that best fits the data, while having a maximum entropy $-\mathrm{Tr}\rho\ln\rho$. We thus make sure that the reconstructed state does not contain more information than that provided by the experimental data. We finally represent the reconstructed density matrix by its Wigner function, which gives a clearer insight into the main features of the states.

Figure 16(a) presents the measured Wigner function of the even cat (preparation atom detected in $|e\rangle$), for $|\gamma| = \sqrt{3.5}$ and $\phi_0 = 0.74\,\pi$. The Wigner function presents two positive bumps centred on the superposed classical amplitudes, $\gamma\exp(\pm i\phi_0/2)$ (the cat's 'ears'). In between these two classical features, we observe a high contrast interference pattern that reveals the quantum nature of the superposition (the cat's 'smile'). The observed Wigner function is quite close to the theoretical expectation (shown in the inset).

The 'size' of this cat is measured by the square of the distance $\mathcal{D}$ between the two classical components in phase space: $\mathcal{D}^2 = 11.8$ photons. The decoherence time scale is expected to be $T_d = 2T_c/\mathcal{D}^2$ at zero temperature. Note that the ears of our cat are not exactly Gaussian (as should be for a superposition of coherent states). This is not due to an imperfection in the reconstruction procedure, but to the cat preparation stage. Since we are not deeply into the dispersive regime (the atom-cavity detuning is $\delta/2\pi = 51$ kHz, not very large compared to $\Omega_0/2\pi$), the phase shift of a Fock state depends in a non-linear way on the photon number, leading to a slight deformation of the coherent components.

Figure 16(b) presents the Wigner function of the odd cat. The classical components are the same, but the interference pattern is phase-shifted by π as compared to that of the even cat. Finally, Fig. 16(c) presents the Wigner function of a statistical

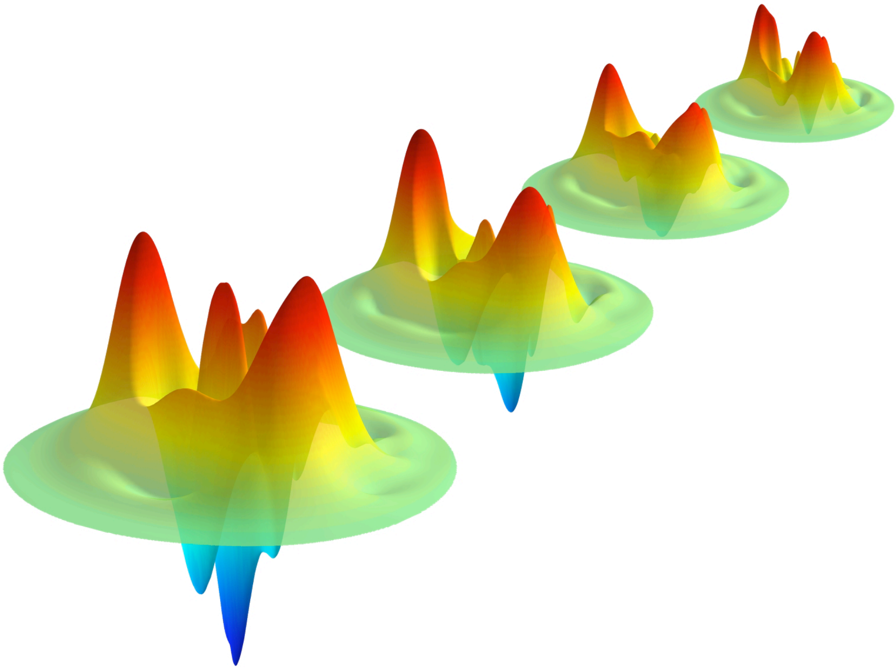

Figure 17: For snapshots of the Wigner function of a decaying Schrödinger cat state. The initial state is the even cat of Fig. 16(a). The snapshots are taken 1.3 ms, 4.3 ms, 15.8 ms and 22.9 ms (from front to back) after cat preparation.

mixture of the two coherent components. It is obtained by mixing data corresponding to different detected states of the preparation atom. The cavity state is then a statistical mixture of the odd and even cat, or equivalently a statistical mixture of the two coherent components. The classical ears are still there, but the smile is gone, as expected.

For the reconstruction of ρ, we can repeat the experiment many times for each β value. We thus use only a few QND atoms in each realization and still achieve good statistics. We chose to detect about 20 atoms in a 4 ms time interval. We are thus able to measure the time evolution of the field state (or of its Wigner function) with a decent time resolution.

Figure 17 presents four snapshots of the even cat Wigner function evolution [the conditions are those of Fig. 16(a)]. The quantum feature, the cat's smile, decays much faster than the energy (the energy decay corresponds to a slow motion of the ears towards the origin, with a time constant $T_c/2$). After about 23 ms, the contrast of the interference pattern is considerably reduced and we are left with a mere statistical mixture. From these data, we deduce the decoherence time scale, T_d, defined as the damping time of the non-diagonal elements of the density matrix in the coherent state basis. We get $T_d = 17 \pm 3$ ms, in excellent agreement with the theoretical expectation, 19.5 ms, taking into account the finite mode temperature.

We get in this way a detailed insight into the cat state decoherence. More precise measurements, with quite larger cats, could allow us to realize a full quantum process tomography of the cavity relaxation. Experiments on 'decoherence metrology' are interesting to test alternative interpretations of the conspicuous lack of quantum superpositions at the macroscopic scale [54].

5 Conclusion

We have briefly described microwave cavity QED experiments which implement some of the thought experiments proposed by Bohr and the founding fathers of the quantum theory. We can trap photons in boxes and weigh them with scales at the atomic level. We are able to count the number of photons in the box without absorbing them in an ideal Quantum Non Demolition measurement of the field intensity. This process directly illustrates all the prescriptions of the Copenhagen interpretation for quantum measurements. We can record which-path information in an atomic interferometer, as with Bohr's thought moving slit device for interfering particles. We directly illustrate the complementarity concept by showing that full which-path information and interference fringes are mutually incompatible.

These experiments lead to the preparation of mesoscopic quantum states and mesoscopic quantum superpositions. The QND measurement process prepares Fock states. We have performed a detailed study of their relaxation. The slow pace of these experiments and the exquisite controllability of the atomic system make it also possible to test strategies to combat decoherence. Quantum feedback uses information extracted by QND probes to deterministically steer the cavity field towards a prescribed Fock state. It also protects these non-classical resources from decoherence by reversing rapidly the adverse effects of quantum jumps.

The complementarity experiment leads to the preparation of a quantum superposition of mesoscopic coherent states, a mesoscopic equivalent of the famous Schrödinger cat. A full quantum state reconstruction procedure, also based on the QND atomic probes, allows us to get a detailed insight into the decoherence of this cat state. These experiments are thus also well suited for the exploration of the boundary between the quantum and the classical worlds.

All these achievements open promising perspectives. One of them involves the interaction of slow circular Rydberg atoms with the cavity. In the present set-up, the atom-cavity interaction time is limited to about 100 μs by the thermal velocity of the atomic beam. This is an asset when we need to extract information rapidly out of the cavity, but it is a severe limitation for other experiments. We are thus developing a new set-up, represented in Fig. 18, where the atoms will be prepared inside the cavity itself, out of a slow atomic beam in a fountain arrangement. Atoms excited near their turning point interact with the mode for times in the millisecond range, only limited by their free fall through the mode's waist. The limited levels lifetime makes it mandatory to perform the field ionization detection also in the cavity structure.

With these long interaction times, we could generate large cat states, containing up to a few tens of photons with high fidelities and monitor their decoherence. We could realize quantum random walks for the phase of the cavity field, driven by a single atom [55]. We could realize engineered reservoirs for the cavity field relaxation, made up of atoms crossing the cavity one by one. We have shown recently that this strategy prepares and stabilizes against mundane decoherence a large class of non-classical states [56, 57].

Finally, the atom-cavity interaction time could be long enough to resolve the anharmonicity of the dressed-levels ladder and to address selectively a transition corresponding to one precise photon number. We have shown recently that we could realize a Quantum Zeno Dynamics (QZD) in this context [58, 59]. QZD [60] gener-

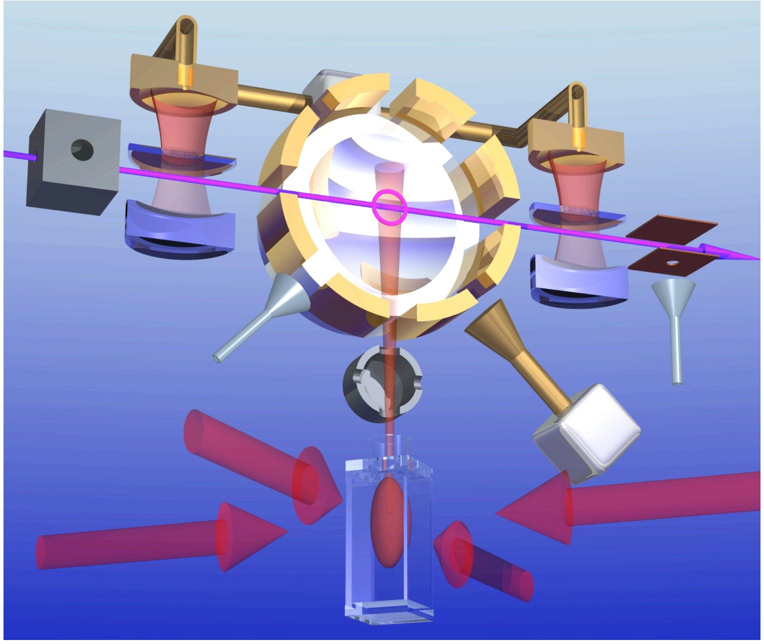

Figure 18: Experimental set-up under construction, featuring a slow atomic beam in a fountain arrangement to prepare circular atoms nearly at rest in a high-Q cavity (only one mirror is shown). The electrodes around the cavity are used for the circular state preparation and field-ionisation detection. A fast horizontal atomic beam with its Ramsey zones and detectors is used for cavity diagnostic.

alizes the Quantum Zeno Effect to measurements of an observable with degenerate eigenspaces. Under such frequently repeated measurements, the system evolution is confined in one of these subspaces, and proceeds under the restriction of the Hamiltonian in the subspace.

Frequent interrogation of a photon-number selective transition in the dressed levels implements such a dynamics, restricting the evolution to photon numbers smaller or larger than the addressed one. This leads to non-trivial dynamics and to the efficient generation of non-classical states. Combining these interrogations with global displacements, we proposed 'phase space tweezers', able to pick out a single coherent component in a complex cat-like superposition and to move it at will, independently from the others. Moreover, these tweezers can be adapted to prepare such superpositions rapidly from the initial vacuum state, a rather fascinating perspective.

References

[1] N. Bohr, *Collected Works* (North Holland, Amsterdam, 1985).

[2] N. Bohr, Nature (London), **121**, 580 (1928).

[3] N. Bohr, in *Albert Einstein, Philosopher Scientist*, edited by A. Schilpp (Open Court, La Salle (IL), 1949) p. 201.

[4] A. Einstein, B. Podolsky, and N. Rosen, Phys. Rev., **47**, 777 (1935).

[5] N. Bohr, Phys. Rev., **48**, 696 (1935).

[6] N. F. Ramsey, *Molecular Beams*, International Series of Monographs on Physics (Oxford University Press, Oxford, 1985).

[7] C. W. Chou, D. B. Hume, T. Rosenband, and D. J. Wineland, Science, **329**, 1630 (2010).

[8] M. Rangaswamy, B. Porejsz, B. A. Ardekani, S. J. Choi, J. L. Tanabe, K. O. Lim, and H. Begleiter, Neuroimage, **21**, 329 (2004).

[9] E. Schrödinger, Naturwissenschaften, **23**, 807, 823, 844 (1935).

[10] S. Haroche and J.-M. Raimond, *Exploring the quantum: atoms, cavities and photons* (Oxford University Press, 2006).

[11] E. M. Purcell, Phys. Rev., **69**, 681 (1946).

[12] H. Mabuchi and A. C. Doherty, Science, **298**, 1372 (2002).

[13] C. Nölleke, A. Neuzner, A. Reiserer, C. Hahn, G. Rempe, and S. Ritter, Phys. Rev. Lett., **110**, 140403 (2013).

[14] K. Hennessy, A. Badolato, M. Winger, D. Gerace, M. Atature, S. Gulde, S. Falt, E. L. Hu, and A. Imamoglu, Nature, **445**, 896 (2007).

[15] M. D. Reed, L. DiCarlo, S. E. Nigg, L. Sun, L. Frunzio, S. M. Girvin, and R. J. Schoelkopf, Nature, **482**, 382 (2012).

[16] E. T. Jaynes and F. W. Cummings, Proc. IEEE, **51**, 89 (1963).

[17] S. Gleyzes, S. Kuhr, C. Guerlin, J. Bernu, S. Deléglise, U. B. Hoff, M. Brune, J.-M. Raimond, and S. Haroche, Nature (London), **446**, 297 (2007).

[18] C. Guerlin, J. Bernu, S. Deléglise, C. Sayrin, S. Gleyzes, S. Kuhr, M. Brune, J.-M. Raimond, and S. Haroche, Nature (London), **448**, 889 (2007).

[19] M. Brune, J. Bernu, C. Guerlin, S. Deléglise, C. Sayrin, S. Gleyzes, S. Kuhr, I. Dotsenko, J.-M. Raimond, and S. Haroche, Phys. Rev. Lett., **101**, 240402 (2008).

[20] C. Sayrin, I. Dotsenko, X. Zhou, B. Peaudecerf, T. Rybarczyk, S. Gleyzes, P. Rouchon, M. Mirrahimi, H. Amini, M. Brune, J.-M. Raimond, and S. Haroche, Nature (London), **477**, 73 (2011).

[21] X. Zhou, I. Dotsenko, B. Peaudecerf, T. Rybarczyk, C. Sayrin, S. Gleyzes, J. M. Raimond, M. Brune, and S. Haroche, Phys. Rev. Lett., **108**, 243602 (2012).

[22] M. Brune, E. Hagley, J. Dreyer, X. Maître, A. Maali, C. Wunderlich, J.-M. Raimond, and S. Haroche, Phys. Rev. Lett., **77**, 4887 (1996).

[23] S. Deléglise, I. Dotsenko, C. Sayrin, J. Bernu, M. Brune, J.-M. Raimond, and S. Haroche, Nature (London), **455**, 510 (2008).

[24] R. G. Hulet and D. Kleppner, Phys. Rev. Lett., **51**, 1430 (1983).

[25] T. F. Gallagher, *Rydberg Atoms* (Cambridge University Press, Cambridge, 1994).

[26] M. Gross and J. Liang, Phys. Rev. Lett., **57**, 3160 (1986).

[27] P. Maioli, T. Meunier, S. Gleyzes, A. Auffeves, G. Nogues, M. Brune, J.-M. Raimond, and S. Haroche, Phys. Rev. Lett., **94**, 113601 (2005).

[28] J. D. Jackson, *Classical Electrodynamics*, 2nd ed. (Wiley, New York, 1975).

[29] P. Nussenzveig, F. Bernardot, M. Brune, J. H. J.-M. Raimond, S. Haroche, and W. Gawlik, Phys. Rev. A, **48**, 3991 (1993).

[30] J.-M. Raimond, M. Brune, and S. Haroche, Rev. Mod. Phys., **73**, 565 (2001).

[31] A. Rauschenbeutel, G. Nogues, S. Osnaghi, P. Bertet, M. Brune, J.-M. Raimond, and S. Haroche, Science, **288**, 2024 (2000).

[32] S. Kuhr, S. Gleyzes, C. Guerlin, J. Bernu, U. B. Hoff, S. Deléglise, S. Osnaghi, M. Brune, J.-M. Raimond, S. Haroche, E. Jacques, P. Bosland, and B. Visentin, Appl. Phys. Lett., **90**, 164101 (2007).

[33] S. M. Barnett and P. M. Radmore, *Methods in Theoretical Quantum Optics* (Oxford University Press, Oxford, 1997).

[34] W. H. Louisell, *Quantum Statistical Properties of Radiation* (Wiley, New York, 1973).

[35] G. Lindblad, Commun. Math. Phys., **48**, 119 (1976).

[36] W. H. Zurek, Rev. Mod. Phys., **75**, 715 (2003).

[37] E. P. Wigner, Phys. Rev., **40**, 749 (1932).

[38] K. E. Cahill and R. J. Glauber, Phys. Rev., **177**, 1857 (1969).

[39] D. M. Greenberger, M. Horne, A. Shimony, and A. Zeilinger, Am. J. Phys., **58**, 1131 (1990).

[40] V. B. Braginskii, Y. I. Vorontsov, and K. S. Thorne, Science, **209**, 547 (1980).

[41] P. Grangier, J. A. Levenson, and J.-P. Poizat, Nature (London), **396**, 537 (1998).

[42] T. Sauter, W. Neuhauser, R. Blatt, and P. Toschek, Phys. Rev. Lett., **57**, 1696 (1986).

[43] J. C. Bergquist, R. G. Hulet, W. M. Itano, and D. J. Wineland, Phys. Rev. Lett., **57**, 1699 (1986).

[44] M. Bauer and D. Bernard, Phys. Rev. A, **84**, 044103 (2011).

[45] H. Wang, M. Hofheinz, M. Ansmann, R. C. Bialczak, E. Lucero, M. Neeley, A. D. O'Connell, D. Sank, J. Wenner, A. N. Cleland, and J. M. Martinis, Phys. Rev. Lett., **101**, 240401 (2008).

[46] B. Misra and E. C. G. Sudarshan, J. Math. Phys., **18**, 756 (1977).

[47] W. M. Itano, D. J. Heinzen, J. J. Bollinger, and D. J. Wineland, Phys. Rev. A, **41**, 2295 (1990).

[48] J. Bernu, C. Deléglise, C. Sayrin, S. Kuhr, I. Dotsenko, M. Brune, J.-M. Raimond, and S. Haroche, Phys. Rev. Lett., **101**, 180402 (2008).

[49] H. M. Wiseman, Phys. Rev. A, **49**, 2133 (1994).

[50] A. C. Doherty, S. Habib, K. Jacobs, H. Mabuchi, and S. M. Tan, Phys. Rev. A, **62**, 012105 (2000).

[51] R. Vijay, C. Macklin, D. H. Slichter, S. J. Weber, K. W. Murch, R. Naik, A. N. Korotkov, and I. Siddiqi, Nature, **490**, 77 (2012).

[52] P. Bertet, S. Osnaghi, A. Rauschenbeutel, G. Nogues, A. Auffeves, M. Brune, J.-M. Raimond, and S. Haroche, Nature (London), **411**, 166 (2001).

[53] V. Buzek and G. Drobny, J. Mod. Opt., **47**, 2823 (2000).

[54] S. Adler and A. Bassi, Science, **325**, 275 (2009).

[55] B. C. Sanders, S. D. Bartlett, B. Tregenna, and P. L. Knight, Phys. Rev. A, **67**, 042305 (2003).

[56] A. Sarlette, J.-M. Raimond, M. Brune, and P. Rouchon, Phys. Rev. Lett., **107**, 010402 (2011).

[57] A. Sarlette, Z. Leghtas, M. Brune, J. M. Raimond, and P. Rouchon, Phys. Rev. A, **86**, 012114 (2012).

[58] J.-M. Raimond, C. Sayrin, S. Gleyzes, I. Dotsenko, M. Brune, S. Haroche, P. Facchi, and S. Pascazio, Phys. Rev. Lett., **105**, 213601 (2010).

[59] J. M. Raimond, P. Facchi, B. Peaudecerf, S. Pascazio, C. Sayrin, I. Dotsenko, S. Gleyzes, M. Brune, and S. Haroche, Phys. Rev. A, **86**, 032120 (2012).

[60] P. Facchi and S. Pascazio, Phys. Rev. Lett., **89**, 080401 (2002).